JOURNAL OF GEOPHYSICAL RESEARCH, VOL. 114, F02004, doi:10.1029/2008JF001015, 2009

The Glimmer community ice sheet model

I. C. Rutt,[1] M. Hagdorn,[2] N. R. J. Hulton,[2] and A. J. Payne[3]

Received 18 March 2008; revised 23 November 2008; accepted 26 January 2009; published 10 April 2009.

[1] We present a detailed description of the Glimmer ice sheet model, comprising the physics represented in the model and the numerical techniques used. Established methods are combined with good software design to yield an adaptable and widely applicable model. A flexible framework for coupling Glimmer to global climate forcing is also described. Testing and benchmarking is of crucial importance if the outputs of numerical models are to be regarded as credible; we demonstrate that Glimmer performs very well against the well-known EISMINT benchmarks and against other analytical solutions for ice flow. Glimmer therefore represents a well-founded and flexible framework for the open-source development of ice sheet modeling.

Citation: Rutt, I. C., M. Hagdorn, N. R. J. Hulton, and A. J. Payne (2009), The Glimmer community ice sheet model, *J. Geophys. Res.*, *114*, F02004, doi:10.1029/2008JF001015.

1. Introduction

1.1. Background

[2] In the last 3 decades, numerical modeling has become established within glaciology as an important technique for the understanding of ice sheet dynamics. Ice sheet models are of particular importance if we are to predict the possible response of ice sheets to climate change, and consequently a number of such models have been developed over the years.

[3] This paper describes a thermomechanical ice sheet model that uses the shallow ice approximation, and is known as Glimmer. The paper focuses on a detailed description of the core thermomechanical model and its verification against established benchmarks. Our purpose is to provide a reference document setting out concisely the physics and numerics of the model, and demonstrating that it passes a set of widely recognized tests.

[4] The name ''Glimmer'' was originally an acronym devised to reflect the model's beginnings as a component of the GENIE earth system model [*Lenton et al.*, 2007], and stands for GENIE Land Ice Model with Multiply-Enabled Regions. However, because Glimmer has developed subsequently as an independent model, the meaning of the name is no longer important, and it is not capitalized.

[5] Use of the shallow ice approximation (SIA) in ice sheet modeling can be traced back to the work of *Mahaffy* [1976] and the thermomechanical model of *Jenssen* [1977]. The applicability of the SIA has been discussed at length elsewhere in the literature [e.g., *Hutter*, 1983; *Hindmarsh and Le Meur*, 2001; *Pattyn*, 2003], and although it lacks representation of higher-order stresses in the ice, it has been shown to perform well compared to full-stress models in a wide range of glaciological situations [e.g., *Leysinger Vieli and Gudmundsson*, 2004]. It is also important as a basis for modeling ice sheet evolution over long time scales because of its computational efficiency: numerous recent studies have used models based on the SIA [e.g., *Calov et al.*, 2005; *Charbit et al.*, 2005; *Abe-Ouchi et al.*, 2007; *Flowers et al.*, 2008], and, accordingly, it continues to be the subject of theoretical analysis [e.g., *Saito and Abe-Ouchi*, 2005; *Van den Berg et al.*, 2006]. Nevertheless, the use of the SIA precludes the simulation of many of the rapid changes now being observed in Greenland and Antarctica.

[6] Given the well-established nature of Glimmer's theoretical foundations and its numerical implementation, it is important to stress the characteristics which distinguish it from its predecessors. First, the model has been verified against a range of established standards, allowing a high degree of confidence to be placed in its output. Second, the software engineering design of the model, and its open development process, have produced model code that is well structured and well documented. The design of the code is such that it is easy to deploy the model in a range of experimental configurations, and to couple it to whatever climate forcing is desired. Finally, Glimmer is supplied with a sophisticated module (called GLINT) which allows coupling to a global climate model or reanalysis data, and which automatically handles the various temporal and spatial transformations necessary. Taken together, these characteristics mean that Glimmer is well suited to the adaption and extension of its capabilities.

[7] All numerical models are approximations to reality: all make compromises for the sake of efficiency and tractability, and, in this, Glimmer is no different. Most significantly, the use of the SIA precludes the direct representation of ice shelf flow, because the stress balance in an ice shelf is dominated by longitudinal and lateral stress gradients, which are absent from the SIA. Some ice sheet models [e.g., *Huybrechts*, 2002] attempt to overcome this by including a separate ice shelf model; however, the difficulties presented by doing so are significant [*Vieli and*

[1]School of the Environment and Society, Swansea University, Swansea, UK.
[2]School of GeoSciences, University of Edinburgh, Edinburgh, UK.
[3]Centre for Polar Observation and Modelling, School of Geographical Sciences, University of Bristol, Bristol, UK.

0148-0227/09/2008JF001015$09.00

Payne, 2005], especially concerning the coupling of the two models across the grounding line. Consequently, Glimmer does not include an ice shelf model at present. Other compromises described below include the simplicity of basal sliding and basal hydrology models, and the parameterization of calving at a marine margin. None of these limitations is unusual in a model of this kind. However, because of Glimmer's status as an open source, community model, and because of the well-structured nature of its code base, it presents a unique opportunity for the coordinated improvement of these aspects. One of the purposes of this paper is to stimulate that development.

1.2. Model Structure

[8] Glimmer is structured on a modular basis, with the modeled processes divided into discrete units. The core thermomechanical ice model forms one such unit (called GLIDE), which takes boundary conditions from three sources: a climate driver provides the upper surface temperature and mass balance fields, an isostasy model provides the lower surface elevation, and a geothermal model provides the geothermal heat flux through the lower ice surface. The thermomechanical model, the geothermal model and the isostasy model are all integral parts of Glimmer, and are described in detail in the first part of the paper, with each component the subject of a separate section. The physics represented and the numerical techniques used are presented together for each component. In contrast, the climate driver can be any model component capable of supplying the required boundary conditions. Several climate drivers are supplied with Glimmer, but the design of Glimmer makes it simple to write new ones. Climate drivers are not discussed in detail here, except in the case of the GLINT module, which allows a global climate model to provide boundary conditions to the ice sheet model (section 6).

1.3. Model Benchmarking

[9] The second major part of the paper concerns the verification of Glimmer against established benchmarks for ice sheet models. We use both of the published EISMINT benchmarks [*Huybrechts et al.*, 1996; *Payne et al.*, 2000], as well as the more recent exact solutions of *Bueler et al.* [2005].

[10] As *Bueler et al.* [2005] note, there is a difference between validation (checking that the correct equations are being solved) and verification (checking that the numerical solution is correct). Our focus in this paper is the verification of Glimmer: the purpose is to show that it solves the relevant equations accurately.

[11] Comparison between the output obtained from Glimmer and the published results show good agreement, and give confidence that the model presented herein has been implemented correctly.

1.4. Development Control and Version Numbers

[12] The Glimmer model code has been developed according to procedures commonly used in open source software development [*Bar and Fogel*, 2003]. Code changes are recorded using the Concurrent Versions System (CVS), in a publicly accessible repository hosted at the UK National eScience Centre (NeSC). The Glimmer project page may be found at http://glimmer.forge.nesc.ac.uk. Glimmer users are encouraged to participate in model development and documentation. The present list of registered developers has fourteen members drawn from six institutions, with many more providing bug reports and code patches.

[13] The model code held on the CVS repository is in a state of continuous development. Prepackaged, numbered releases of the model are made at regular intervals, and these can be freely downloaded from the NeSC project Web site. Comprehensive documentation can be downloaded from the same source. A release collects together developments to the model as a single snapshot, making it easier for users and developers to keep track of changes. This paper concerns itself with the latest release in the 1.0.*x* series, which is the stable development branch. Changes in 1.0.*x* are restricted to bug fixes or minor enhancements to existing features; the latest release version is 1.0.14. In addition, a more experimental development branch is maintained, where new features can be implemented and tested, and whose versions are numbered 1.5.0 upward. This paper does not concern itself with these developments.

[14] Note that releases are always given even version numbers, such as 1.0.2, 1.0.4, etc. The state of the CVS repository between releases is assigned a notional odd version number, such as 1.0.3, 1.0.5, etc.

2. Thermomechanical Ice Sheet Model (GLIDE)

[15] The core of Glimmer is the thermomechanical ice sheet model, known as GLIDE (Glimmer Ice Dynamics Element). The model code of GLIDE is based on that described by *Payne* [1999], but has undergone sufficient revision that a full description of the model is presented here, for clarity. The values and symbols of all physical constants and other parameters found in the model description are listed together in Table 1.

2.1. Ice Sheet Mechanics

[16] The evolution of the ice thickness stems from the continuity equation for an incompressible material

$$\nabla \cdot \mathbf{u} + \frac{\partial w}{\partial z} = 0, \tag{1}$$

where ∇ is the horizontal gradient operator, $\mathbf{u} = (u, v)$ is the horizontal velocity, and w is the vertical velocity. The vertical coordinate z is positive upward. In the equations that follow, h is the elevation of the bed, s is the elevation of the ice surface, and $H = s - h$ is the ice thickness. By integrating through the ice thickness, equation (1) can be expressed as

$$\frac{\partial H}{\partial t} = -\nabla \cdot (\bar{\mathbf{u}} H) + b - S, \tag{2}$$

where b is the surface mass balance rate and S is the basal melt rate [*Payne and Dongelmans*, 1997]. Note that the signs of b and S are different.

[17] As noted in the introduction, and in common with other large-scale ice sheet models, the shallow ice approximation (SIA) is used. The SIA assumes that bedrock and

Table 1. List of Physical Constants and Their Default Values

Symbol	Description	Value	Units
a	material constant		
	for $T^* \geq 263$K	$1.733 \cdot 10^3$	$\text{Pa}^{-3}\text{s}^{-1}$
	for $T^* < 263$K	$3.613 \cdot 10^{-13}$	$\text{Pa}^{-3}\text{s}^{-1}$
c_{ice}	specific heat capacity of ice	2009	$\text{J kg}^{-1}\text{K}^{-1}$
c_{rock}	specific heat capacity of rock	1000	$\text{J kg}^{-1}\text{K}^{-1}$
g	acceleration due to gravity	9.81	ms^{-2}
H_{rock}	thickness of rock layer	5	km
k_{ice}	thermal conductivity of ice	2.1	$\text{W m}^{-1}\text{K}^{-1}$
k_{rock}	thermal conductivity of rock	3.3	$\text{W m}^{-1}\text{K}^{-1}$
L	specific latent heat of fusion	$335 \cdot 10^3$	J kg^{-1}
n	flow law exponent	3	
Q	activation energy for creep		
	for $T^* \geq 263$K	$139 \cdot 10^3$	J mol^{-1}
	for $T^* < 263$K	$60 \cdot 10^3$	J mol^{-1}
R	universal gas constant	8.314	$\text{J mol}^{-1}\text{K}^{-1}$
ρ_{ast}	density of mantle	3300	kg m^{-3}
ρ_{i}	density of ice	910	kg m^{-3}
ρ_{rock}	density of rock	3300	kg m^{-3}
ρ_{sw}	density of seawater	1028	kg m^{-3}
ρ_{w}	density of fresh water	1000	kg m^{-3}
C_T	dependence of melting point on pressure	$9.76 \cdot 10^{-8}$	K Pa^{-1}
L_G	atmospheric temperature lapse rate	8	K km^{-1}
	tolerance of nonlinear scheme	2	mm
	maximum number of Picard iterations	50	

ice surface slopes are sufficiently small that the normal stress components can be neglected [*Hutter*, 1983]. This means that the horizontal shear stresses (τ_{xz} and τ_{yz}) can be approximated by

$$\tau_{xz}(z) = -\rho_{\text{i}} g (s - z) \frac{\partial s}{\partial x}, \tag{3}$$

and

$$\tau_{yz}(z) = -\rho_{\text{i}} g (s - z) \frac{\partial s}{\partial y}, \tag{4}$$

where ρ_{i} is the density of ice and g the acceleration due to gravity.

[18] Strain rates $\dot{\epsilon}_{ij}$ of polycrystalline ice are related to the stress tensor by the nonlinear flow law [*Glen*, 1952; *Nye*, 1953]. Using the SIA, we obtain

$$\dot{\epsilon}_{xz} = \frac{1}{2}\left(\frac{\partial u}{\partial z} + \frac{\partial w}{\partial x}\right) = A(T^*)\tau_*^{(n-1)}\tau_{xz}, \tag{5}$$

with an equivalent expression for $\dot{\epsilon}_{yz}$. In equation (5), n is the flow law exponent, A is the temperature-dependent flow law coefficient, and τ_* is the effective shear stress. The values of $\partial w/\partial x$ and $\partial w/\partial y$ are taken to be small compared to the other terms. The effective shear stress τ_* is given by the second invariant of the stress tensor; for the SIA, this is

$$\tau_* = \left(\tau_{xz}^2 + \tau_{yz}^2\right)^{\frac{1}{2}}. \tag{6}$$

By combining equations (3), (4), (5) and (6), an expression for the vertical gradient of $\mathbf{u}$ may be obtained

$$\frac{\partial \mathbf{u}}{\partial z} = -2A(T^*)(\rho_{\text{i}} g (s - z))^n |\nabla s|^{n-1} \nabla s. \tag{7}$$

The temperature T^* is the absolute temperature corrected for the dependence of the melting point on pressure, so that

$$T^* = T + \rho_{\text{i}} g C_T (s - z), \tag{8}$$

with T in Kelvin [*Huybrechts*, 1986] and C_T a constant, given in Table 1. The parameters A and n must be determined empirically: the value of the flow law exponent n is not very well constrained by experiment, but is conventionally taken to be 3 in ice sheet modeling [*Paterson*, 1994]. The scaling coefficient A depends on factors such as temperature, crystal size and orientation, and ice impurities. Experiments suggest that A follows the Arrhenius relationship

$$A(T^*) = f a e^{-Q/RT^*}, \tag{9}$$

where a is a temperature-independent material constant, Q is the activation energy for creep and R is the universal gas constant [*Paterson*, 1994]. The tuning parameter f can be used to "speed up" ice flow, and accounts for ice impurities and the development of anisotropic ice fabrics [*Payne*, 1999; *Tarasov and Peltier*, 1999, 2000; *Peltier et al.*, 2000].

[19] Integrating (7) with respect to z gives the horizontal velocity profile

$$\mathbf{u}(z) - \mathbf{u}(h) = -2(\rho_{\text{i}} g)^n |\nabla s|^{n-1} \nabla s \int_h^z A (s - z')^n dz', \tag{10}$$

where $\mathbf{u}(h)$ is the basal, or sliding, velocity. Integrating (10) again with respect to z gives an expression for the vertically averaged ice velocity $\overline{\mathbf{u}}$

$$\overline{\mathbf{u}} = -\frac{2}{H}(\rho_{\text{i}} g)^n |\nabla s|^{n-1} \nabla s \int_h^s \int_h^z A (s - z')^n dz' dz + \mathbf{u}(h). \tag{11}$$

The basal velocity $\mathbf{u}(h)$ is taken to be proportional to the basal shear stress [*Payne*, 1995]

$$\mathbf{u}(h) = -B \rho_{\text{i}} g H \nabla s. \tag{12}$$

The sliding parameter B may be determined by a number of different methods, described in section 2.2 below.

[20] The vertical ice velocity can be found by integrating (1) with respect to z, to give the vertical velocity distribution of each ice column

$$w(z) = -\int_h^z \nabla \cdot \mathbf{u}(z') dz' + w(h). \tag{13}$$

The lower, kinematic boundary condition is [*Hindmarsh and Hutter*, 1988]

$$w(h) = \frac{\partial h}{\partial t} + \mathbf{u}(h) \cdot \nabla h - S, \tag{14}$$

with the basal melt rate S calculated as discussed in section 2.3 below, and given by equation (24). The upper kinematic boundary is similarly formulated, and must satisfy

$$w(s) = \frac{\partial s}{\partial t} + \mathbf{u}(s) \cdot \nabla s - b. \tag{15}$$

2.2. Basal Sliding

[21] The basal sliding parameter B may be specified in a number of forms: (1) no sliding, $B = 0$; (2) constant sliding parameter, which may vary spatially, $B = B_0(x, y)$; (3) constant sliding parameter, which may vary spatially, only when the basal temperature is equal to the pressure melting point,

$$B = \begin{cases} B_0(x,y) & \text{if} \quad T = T_{\text{pmp}} \\ 0 & \text{if} \quad T < T_{\text{pmp}} \end{cases}; \tag{16}$$

(4) constant sliding parameter, which may vary spatially, only in the presence of basal water (depth denoted d_w),

$$B = \begin{cases} B_0(x,y) & \text{if} \quad d_w > 0 \\ 0 & \text{if} \quad d_w = 0 \end{cases}. \tag{17}$$

and (5) sliding parameter that is proportional to the basal melt rate, up to a maximum value,

$$B = \begin{cases} \min(B_{\max}, B_0(x,y) + \alpha_B S) & \text{if} \quad S > 0 \\ 0 & \text{if} \quad S = 0 \end{cases}, \tag{18}$$

where α_B is a constant of proportionality.

[22] Note that the methods which depend on the basal temperature and the presence of basal meltwater are not equivalent: although the bed temperature may be at the pressure melting point, there may not be enough excess energy to produce melt, or the meltwater may be removed by the basal hydrology (see section 2.4 below).

2.3. Thermodynamics

[23] The flow law, equation (5), depends on the temperature of ice. Therefore, it is necessary to determine how the distribution of ice temperature changes with a changing ice sheet configuration. The thermal evolution of the ice sheet is described by

$$\frac{\partial T}{\partial t} = \frac{k}{\rho_i c}\left(\nabla^2 T + \frac{\partial^2 T}{\partial z^2}\right) - \mathbf{u} \cdot \nabla T + \frac{\Phi}{\rho_i c} - w\frac{\partial T}{\partial z}, \tag{19}$$

where T is the absolute temperature, k is the thermal conductivity of ice, c is the specific heat capacity and Φ is the heat generated because of internal friction.

[24] The internal heating rate per unit volume is

$$\Phi = \sum_{i,j} \dot{\epsilon}_{ij}\tau_{ij}. \tag{20}$$

Assuming that heating due to longitudinal strain rates is small compared with that due to horizontal shear strain rates, equation (20) can be simplified to [*Huybrechts*, 1986]

$$\begin{aligned} \Phi &= 2\dot{\epsilon}_{xz}\tau_{xz} + 2\dot{\epsilon}_{yz}\tau_{yz} \\ &= -\rho_i g(s-z)\frac{\partial \mathbf{u}}{\partial z} \cdot \nabla s. \end{aligned} \tag{21}$$

[25] At the upper boundary, ice temperatures are set to the mean annual surface temperature, T_{surf}. The ice at the base is heated by the geothermal heat flux and sliding friction

$$\left.\frac{\partial T}{\partial z}\right|_{z=h} = -\frac{G + \boldsymbol{\tau}_b \cdot \mathbf{u}(h)}{k}, \tag{22}$$

where $\mathbf{u}(h)$ is the basal ice velocity, and the basal shear stress $\boldsymbol{\tau}_b$ is obtained from equations (3) and (4), so that $\boldsymbol{\tau}_b = -\rho_i g H \nabla s$. The geothermal heat flux G can be computed using the geothermal heat flux model outlined in section 3. Ice temperatures are held constant if they reach the pressure melting point of ice, i.e.,

$$T = T_{\text{pmp}} \quad \text{if} \quad T \geq T_{\text{pmp}}. \tag{23}$$

Excess heat is then used to formulate a basal mass balance rate, S

$$S = \frac{k}{\rho_i L}\left(\frac{\partial T^*}{\partial z} - \frac{\partial T}{\partial z}\right), \tag{24}$$

where L is the specific latent heat of fusion. Finally, basal temperatures are held constant at the pressure melting point if the ice is floating

$$T(h) = T_{\text{pmp}}(h). \tag{25}$$

2.4. Basal Hydrology

[26] Two simple models of basal hydrology are provided. Neither of these models represents the evolution of basal water depth in a very realistic fashion: they are included here for completeness, and because the calculation of basal water depth is required by some of the models of basal sliding described above.

2.4.1. Local Water Balance

[27] Water is generated according to the local melt rate S, and assumed to be transported out of the system over a prescribed time scale λ_w. Horizontal advection of meltwater is not modeled, so that

$$\frac{\partial d_w}{\partial t} = S - \frac{d_w}{\lambda_w}. \tag{26}$$

[28] This equation is solved using an implicit time step Δt_w, so that

$$\frac{d_w^{t+1} - d_w^t}{\Delta t_w} = S - \frac{d_w^{t+1} + d_w^t}{2\lambda_w}. \tag{27}$$

The superscript t indicates the relevant time step.

2.4.2. Local Water Balance With Advection

[29] Water is generated according to the local model rate S, and routed under the ice sheet according to a rudimentary flow model. In areas where the basal temperature is equal to the pressure melting point, the water pressure potential ϕ_w at the bed of the ice sheet is given by [*Paterson*, 1994]

$$\phi_w = \rho_w(h + d_w) + \rho_i g H. \tag{28}$$

The magnitude of the subglacial water velocity $|\mathbf{u}_w|$ is assumed to be constant (analogous with the meltwater removal time scale λ_w). The direction of water flow is given by the slope of the potential surface ϕ_w, giving the following advection equation

$$\frac{\partial d_w}{\partial t} = \frac{|\mathbf{u}_w|}{|\nabla \phi_w|} \nabla \phi_w \cdot \nabla d_w. \tag{29}$$

The advection equation is solved using the Lax-Wendroff method.

2.5. Margin Processes

[30] As noted earlier, Glimmer does not include a representation of ice shelf flow. However, it is still necessary to represent somehow the flow of ice over the grounding line, and its eventual removal by calving processes. From a dynamical perspective, all ice within Glimmer is considered to be grounded; the following parameterizations are available to remove ice at the margin: (1) Remove all floating ice and set $H = 0$ wherever $h < (\rho_i/\rho_{sw})H$, where the density of seawater is denoted ρ_{sw}; (2) reduce the thickness of floating ice by a specified fraction; (3) set $H = 0$ wherever the instantaneous bedrock elevation h is below a specified depth; and (4) set $H = 0$ wherever the unloaded bedrock h_0 is below a specified depth.

2.6. Horizontal Grid

[31] The modeled region ($x \in [0, L_x]$, $y \in [0, L_y]$) is discretized using a regular grid so that $x_i = (i - 1)\Delta x$ for $i \in [1, N_x]$, and similarly for y_j; this is the (i, j) grid. The model uses an additional horizontal grid, denoted (r, s), in order to improve numerical stability [*Huybrechts et al.*, 1996]. Both grids use the same grid spacing, Δx and Δy, but are offset by half a grid spacing. Quantities calculated on the (r, s) grid are denoted with a tilde, e.g., $\tilde{F}$. Quantities are transformed between grids by averaging over the surrounding nodes, so that

$$\begin{aligned} \tilde{F}_{r,s} &= \tilde{F}_{i+\frac{1}{2},j+\frac{1}{2}} \\ &= \tfrac{1}{4}\left(F_{i,j} + F_{i+1,j} + F_{i+1,j+1} + F_{i,j+1}\right), \end{aligned} \tag{30}$$

and

$$\begin{aligned} F_{i,j} &= F_{r-\frac{1}{2},s-\frac{1}{2}} \\ &= \frac{1}{4}\left(\tilde{F}_{r-1,s-1} + \tilde{F}_{r,s-1} + \tilde{F}_{r,s} + \tilde{F}_{r-1,s}\right). \end{aligned} \tag{31}$$

[32] In general, horizontal velocities and associated quantities like the diffusivity are calculated on the (r, s) grid; ice thickness, temperatures and vertical velocities are calculated on the (i, j) grid.

[33] Horizontal gradients are calculated on the (r, s) grid, such that surface gradients are

$$\left(\frac{\partial s}{\partial x}\right)_{r,s} = \tilde{s}^x_{r,s} = \frac{s_{i+1,j} - s_{i,j} + s_{i+1,j+1} - s_{i,j+1}}{2\Delta x}, \tag{32}$$

$$\left(\frac{\partial s}{\partial y}\right)_{r,s} = \tilde{s}^y_{r,s} = \frac{s_{i,j+1} - s_{i,j} + s_{i+1,j+1} - s_{i+1,j}}{2\Delta y}. \tag{33}$$

Ice thickness gradients, $\tilde{H}^x_{r,s}$ and $\tilde{H}^y_{r,s}$, are formed similarly.

2.7. The σ Coordinate System and Vertical Grid Spacing

[34] The vertical coordinate, z, is scaled by the ice thickness analogous to the s coordinate in numerical weather simulations [e.g., *Holton*, 1992]. A new vertical coordinate, σ, is introduced so that the ice surface is at $\sigma = 0$ and the ice base at $\sigma = 1$

$$\sigma = \frac{s - z}{H}. \tag{34}$$

[35] The discretization of the vertical coordinate is generalized to employ an irregular spacing, to reflect the fact that ice flow is more variable at the bottom of the ice column. In the vertical, the index k is used, with $1 \le k \le N_\sigma$. Any distribution of levels may be specified, but, by default, the spacing is given by

$$\sigma_k = \frac{4}{3}\left[1 - \left(\frac{k-1}{N_\sigma - 1} + 1\right)^{-2}\right]. \tag{35}$$

This yields levels spaced most closely together near the base of the ice sheet, where the vertical shear is greatest.

[36] The σ coordinate transformation leads to expressions for spatial and temporal derivatives in the new system, similar to those given by *Hindmarsh and Hutter* [1988] and *Hindmarsh* [1999]. The most important are

$$\frac{\partial f}{\partial t} = \frac{\partial f}{\partial t'} + \frac{1}{H}\left(\frac{\partial s}{\partial t} - \sigma \frac{\partial H}{\partial t}\right)\frac{\partial f}{\partial \sigma}, \tag{36}$$

$$\nabla f = \hat{\nabla} f + \frac{1}{H}(\nabla s - \sigma \nabla H)\frac{\partial f}{\partial \sigma}, \tag{37}$$

$$\frac{\partial f}{\partial z} = -\frac{1}{H}\frac{\partial f}{\partial \sigma}, \tag{38}$$

where, in the σ coordinate system, $\hat{\nabla}$ denotes the horizontal derivative, and t' is time.

[37] The vertical integral of f becomes in the σ coordinate system

$$\int_h^z f(z')dz' = -H\int_1^\sigma f(\sigma')d\sigma', \tag{39}$$

which, combined with (13) and (37), leads to the following expression for the vertical velocity

$$w(\sigma) = \int_1^\sigma \left(H\hat{\nabla}\cdot\mathbf{u} + (\nabla s - \sigma' \nabla H)\frac{\partial \mathbf{u}}{\partial \sigma'}\right)d\sigma' + w(1). \tag{40}$$

In some rare circumstances, discussed in section 7.1 below, the horizontal and vertical discretization used in the model can cause inaccuracies in the evaluation of (40). Because the vertical velocities are important in the calculation of the temperature field, it may be desirable to rescale the vertical velocity such that it is constrained by the upper kinematic

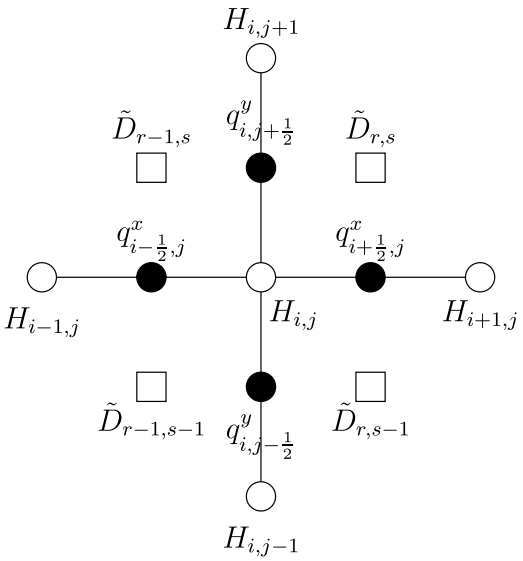

Figure 1. Relationship between discretized ice thicknesses, diffusivities, and mass fluxes. The symbols are explained in the text.

boundary condition (15). In this case, the corrected velocities $w^*(\sigma)$ are given by

$$w^*(\sigma) = w(\sigma) + (1-\sigma)\left(\frac{\partial s}{\partial t} - b + \mathbf{u}(0)\cdot\nabla s - w(0)\right). \quad (41)$$

2.8. Ice Thickness Solver

[38] Equation (2) can be rewritten as a diffusion equation, with a nonlinear diffusion coefficient D

$$\frac{\partial H}{\partial t} = -\nabla\cdot\mathbf{q} + b - S = -\nabla\cdot(D\nabla s) + b - S, \quad (42)$$

with D obtained from (11)

$$D = -2(\rho_i g)^n |\nabla s|^{n-1} \int_h^s \int_h^z A(s-z')^n dz' dz - B\rho_i g H^2. \quad (43)$$

Various methods for discretizing (42) are possible, and are discussed by *Huybrechts et al.* [1996], *Hindmarsh and Payne* [1996], and *Saito and Abe-Ouchi* [2005], among others. The choice made depends on balancing the desire for numerical stability against the higher level of numerical diffusion this can entail. The method chosen for use in Glimmer has a smaller computational molecule (the size of the grid stencil used to evaluate a single point) than some, and this results in lower numerical diffusion [*Hindmarsh and Payne*, 1996]. The computational molecule is also symmetrical: concerns about pattern formation in ice flow [*Payne et al.*, 2000], and knowledge about numerical influences on this patterning suggest that a symmetric scheme should be used. Consequently, care needs to be taken to ensure the time step is kept short enough to maintain numerical stability. The significant speed improvements seen in computer hardware over the past decade serve to ameliorate this possible disadvantage. The implications that the choice of discretization has for the comparison of model outputs with the EISMINT benchmarks are discussed in section 7.1 below.

[39] The diffusion coefficient is calculated on the (r, s) grid, i.e., staggered in both x and y direction. Figure 1 illustrates the arrangement of variables on the staggered grid. Using finite differences, the fluxes in the x direction, q^x, become

$$q^x_{i+\frac{1}{2},j} = -\frac{1}{2}\left(\tilde{D}_{r,s} + \tilde{D}_{r,s-1}\right)\frac{s_{i+1,j} - s_{i,j}}{\Delta x}. \quad (44)$$

The discretization of the ice surface gradient in equation (44) differs from the one given in equation (32) because the fluxes are computed halfway between nodes on the (i, j) grid (see also Figure 1). The fluxes in the y direction, q^y, are analogous.

[40] Glimmer supports three different ways of solving equation (42): an alternating direction implicit method (ADI), a linearized semi-implicit method, and a nonlinear scheme. These are formulated as follows:

[41] 1. The alternating direction implicit method uses the concept of operator splitting where equation (42) is first solved in the x direction and then in the y direction [*Press et al.*, 1992]. The time step Δt is divided into two time steps $\Delta t/2$. The discretized version of equation (42) becomes [*Huybrechts*, 1986]

$$2\frac{H^{t+\frac{1}{2}}_{i,j} - H^t_{i,j}}{\Delta t} = -\frac{q^{x,t+\frac{1}{2}}_{i+\frac{1}{2}j} - q^{x,t+\frac{1}{2}}_{i-\frac{1}{2}j}}{\Delta x} - \frac{q^{y,t}_{i,j+\frac{1}{2}} - q^{y,t}_{i,j-\frac{1}{2}}}{\Delta y} + b_{i,j} - S_{i,j}, \quad (45)$$

$$2\frac{H^{t+1}_{i,j} - H^{t+\frac{1}{2}}_{i,j}}{\Delta t} = -\frac{q^{x,t+\frac{1}{2}}_{i+\frac{1}{2}j} - q^{x,t+\frac{1}{2}}_{i-\frac{1}{2}j}}{\Delta x} - \frac{q^{y,t+1}_{i,j+\frac{1}{2}} - q^{y,t+1}_{i,j-\frac{1}{2}}}{\Delta y} + b_{i,j} - S_{i,j}. \quad (46)$$

The t and $t+\frac{1}{2}$ superscripts indicate the time step concerned. Gathering all $t+\frac{1}{2}$ terms on the left side, equation (45) can be expressed as a tridiagonal set of equations for each row j and column i.

[42] 2. The linearized semi-implicit method uses the Crank-Nicolson scheme. Equation (42) is linearized by calculating the diffusivities in the forward term from the ice thicknesses at the present time step, so that, for example

$$q^{x,t+1}_{i+\frac{1}{2}j} = -\frac{1}{2}\left(\tilde{D}^t_{r,s} + \tilde{D}^t_{r,s-1}\right)\frac{s^{t+1}_{i+1,j} - s^{t+1}_{i,j}}{\Delta x}, \quad (47)$$

with $q^{x,t+1}_{i-\frac{1}{2}j}$, etc, defined analogously. Equation (42) therefore becomes

$$\frac{H^{t+1}_{i,j} - H^t_{i,j}}{\Delta t} = \frac{q^{x,t+1}_{i+\frac{1}{2}j} - q^{x,t+1}_{i-\frac{1}{2}j}}{2\Delta x} + \frac{q^{y,t+1}_{i,j+\frac{1}{2}} - q^{y,t+1}_{i,j-\frac{1}{2}}}{2\Delta y} + \frac{q^{x,t}_{i+\frac{1}{2}j} - q^{x,t}_{i-\frac{1}{2}j}}{2\Delta x} + \frac{q^{y,t}_{i,j+\frac{1}{2}} - q^{y,t}_{i,j-\frac{1}{2}}}{2\Delta y} + b_{i,j} - S_{i,j}. \quad (48)$$

Collecting all H^{t+1} terms of (48) on the LHS and moving all other terms to the RHS we can rewrite (48) as

$$-\alpha_{i,j}H^{t+1}_{i-1,j} - \beta_{i,j}H^{t+1}_{i+1,j} - \gamma_{i,j}H^{t+1}_{i,j-1} - \delta_{i,j}H^{t+1}_{i,j+1} + \left(1-\epsilon_{i,j}\right)H^{t+1}_{i,j} = \zeta_{i,j}, \tag{49}$$

with the RHS

$$\zeta_{i,j} = \alpha_{i,j}H^{t}_{i-1,j} + \beta_{i,j}H^{t}_{i+1,j} + \gamma_{i,j}H^{t}_{i,j-1} + \delta_{i,j}H^{t}_{i,j+1} + \left(1+\epsilon_{i,j}\right)H^{t}_{i,j} + 2\Big(\alpha_{i,j}h_{i-1,j} + \beta_{i,j}h_{i+1,j} + \gamma_{i,j}h_{i,j-1} + \delta_{i,j}h_{i,j+1} + \epsilon_{i,j}h_{i,j}\Big) + b_{i,j}\Delta t - S_{i,j}\Delta t, \tag{50}$$

and the elements of the sparse matrix

$$\alpha_{i,j} = \frac{\tilde{D}_{r-1,s} + \tilde{D}_{r-1,s-1}}{4\Delta x^2}\Delta t, \tag{51}$$

$$\beta_{i,j} = \frac{\tilde{D}_{r,s} + \tilde{D}_{r,s-1}}{4\Delta x^2}\Delta t, \tag{52}$$

$$\gamma_{i,j} = \frac{\tilde{D}_{r,s-1} + \tilde{D}_{r-1,s-1}}{4\Delta y^2}\Delta t, \tag{53}$$

$$\delta_{i,j} = \frac{\tilde{D}_{r,s} + \tilde{D}_{r-1,s}}{4\Delta y^2}\Delta t, \tag{54}$$

$$\epsilon_{i,j} = -\Big(\alpha_{i,j} + \beta_{i,j} + \gamma_{i,j} + \delta_{i,j}\Big). \tag{55}$$

The matrix equation (49) is solved using an iterative matrix solver for nonsymmetric sparse matrices. The solver used here is the biconjugate gradient method with incomplete LU decomposition preconditioning provided by the SLAP package [*Seager*, 1988].

[43] 3. The nonlinearity of equation (42) arises from the dependence of D on s and H. A nonlinear scheme for (42) can be formulated using Picard iteration, which consists of two iterations: an outer, nonlinear and an inner, linear equation. The scheme is started off with the diffusivity from the previous time step, i.e.,

$$D^{(0),t+1} = D^{t}. \tag{56}$$

For each time step, equation (48) is solved multiple times with diffusivities recalculated from the previous iteration

$$D^{(\xi),t+1} = -2(\rho_i g)^n \left|\nabla s^{(\xi-1),t+1}\right|^{n-1} \cdot \int_h^{s^{(\xi-1),t+1}} \int_h^z A\Big(s^{(\xi-1),t+1} - z'\Big)^n dz'dz.$$

The fluxes become (compare with equation (47))

$$q^{x,(\xi),t+1}_{i+\frac{1}{2},j} = -\frac{1}{2}\left(\tilde{D}^{(\xi),t+1}_{r,s} + \tilde{D}^{(\xi),t+1}_{r,s-1}\right)\frac{s^{(\xi),t+1}_{i+1,j} - s^{(\xi),t+1}_{i,j}}{\Delta x}. \tag{57}$$

In these equations, the superscript in brackets (ξ) indicates the iteration number. This procedure is repeated until the maximum ice thickness residual is smaller than some threshold, H_{res}

$$\max\left(\left|H^{(\xi+1),t+1} - H^{(\xi),t+1}\right|\right) < H_{\mathrm{res}}, \tag{58}$$

or the maximum number of iterations is reached. The default values of both quantities are given in Table 1.

2.9. Temperature Solver

[44] In the σ coordinate system, equation (19), becomes

$$\frac{\partial T}{\partial t'} = \frac{k}{\rho_i c H^2}\frac{\partial^2 T}{\partial \sigma^2} - \mathbf{u}\cdot\hat{\nabla}T + \frac{\sigma g}{c}\frac{\partial \mathbf{u}}{\partial \sigma}\cdot\nabla s + \frac{1}{H}\frac{\partial T}{\partial \sigma}\left(w - w_{\mathrm{grid}}\right). \tag{59}$$

Horizontal diffusion is assumed to be negligible [*Paterson*, 1994]. The vertical diffusion and the vertical advection terms (terms 1 and 4) are solved using finite differences for non-equally-spaced nodes. The heat generation term (term 3) is evaluated using the previously found surface slopes and flow factors. The horizontal advection term (term 2) is found using an up-winding scheme [e.g., *Press et al.*, 1992]. Terms arising from the transformation of the horizontal and the time derivatives to the σ coordinate system are combined in the w_{grid} term, which can be thought of as the vertical velocity of the grid

$$w_{\mathrm{grid}}(\sigma) = \frac{\partial s}{\partial t} + \mathbf{u}\cdot\nabla s - \sigma\left(\frac{\partial H}{\partial t} + \mathbf{u}\cdot\nabla H\right). \tag{60}$$

[45] Equation (59) is solved iteratively for each column of ice: temperatures which are not in the column under consideration (these arise from the horizontal advection term) are taken from the previous iteration. The remaining unknown temperatures of the column are discretized using the time-implicit Crank-Nicolson method to form a tridiagonal matrix equation. After each iteration, temperatures are constrained to be less than or equal to the pressure melting temperature of ice. This scheme converges within a small number of iterations (usually 2) and has the advantage of being less complex than considering the full polythermal problem [e.g., *Greve*, 1997].

3. Geothermal Heat Flux Model

[46] The value of the geothermal heat flux G may be specified as a global constant or a spatially varying field within Glimmer; this is common practice in ice sheet modeling. However, a more realistic thermal bedrock model based on the model developed by *Ritz* [1987] is also supplied. This model takes the thermal evolution of the uppermost bedrock layer into account. If the ice is frozen to the ground, temperature perturbations penetrate the bedrock.

This means that the heat flux across the basal boundary depends on past temperature variations [*Ritz*, 1987].

[47] The heat equation for the bedrock layer in the same coordinate system as equation (19) is given by the diffusion equation

$$\frac{\partial T}{\partial t} = \frac{k_{\text{rock}}}{\rho_{\text{rock}} c_{\text{rock}}} \left(\nabla^2 T + \frac{\partial^2 T}{\partial z^2} \right), \tag{61}$$

where k_{rock} is the thermal conductivity, ρ_{rock} the density and c_{rock} the specific heat capacity of the bedrock layer.

[48] We assume that the bedrock temperature does not vary outside the domain of investigation, i.e., the lateral boundary conditions are given by

$$\left.\frac{\partial T}{\partial x}\right|_{x=0} = \left.\frac{\partial T}{\partial x}\right|_{x=L_x} = \left.\frac{\partial T}{\partial y}\right|_{y=0} = \left.\frac{\partial T}{\partial y}\right|_{y=L_y} = 0. \tag{62}$$

[49] At the ice/bedrock interface, three possibilities are considered: (1) If the ice is frozen to the bedrock, the heat flux of the rock layer has to be matched with the heat flux in the basal ice layer, i.e.,

$$k_{\text{rock}} \left.\frac{\partial T}{\partial z}\right|_{z=h^-} = k_{\text{ice}} \left.\frac{\partial T}{\partial z}\right|_{z=h^+}. \tag{63}$$

(2) If the basal ice temperature has reached the pressure melting point of ice, excess heat is used to formulate a melt rate similar to equation (24),

$$S = \frac{1}{\rho_i L} \left(k_{\text{ice}} \left.\frac{\partial T^*}{\partial z}\right|_{z=h+} - k_{\text{rock}} \left.\frac{\partial T}{\partial z}\right|_{z=h^-} + \tau_b \cdot \mathbf{u}(h) \right). \tag{64}$$

(3) The bedrock temperature is set to the surface temperature if there is no ice present.

[50] Initial conditions for the temperature field T are found by applying the geothermal heat flux G to an initial surface temperature T_0

$$T(x, y, z) = T_0 + \frac{G}{k_{\text{rock}}} z. \tag{65}$$

This ensures that initially the geothermal heat flux experienced by the ice sheet is equal to the regional heat flux. The temperature at the base of the bedrock layer is kept constant, i.e.,

$$T(x, y, H_{\text{rock}}) = T_0 + \frac{G}{k_{\text{rock}}} H_{\text{rock}}. \tag{66}$$

[51] Glimmer solves equation (61) in the same way as equation (59), in a vertically scaled coordinate system if horizontal diffusion is neglected. If horizontal diffusion is included, equation (61) is solved using the biconjugate gradient method with incomplete LU decomposition preconditioning.

4. Isostasy Model

[52] The Earth can be treated to a first approximation as a thin elastic layer floating on top of a highly viscous asthenosphere. Earth models can be differentiated by how the two layers are treated [*Le Meur and Huybrechts*, 1996]. The lithosphere can be described as (1) local lithosphere, where the flexural rigidity of the lithosphere is ignored (this is equivalent to ice floating directly on the asthenosphere), or (2) elastic lithosphere, where the flexural rigidity is taken into account. The asthenosphere can be treated as (1) fluid asthenosphere, where the mantle behaves like a nonviscous fluid (isostatic equilibrium is reached instantaneously), or (2) relaxing asthenosphere, where the flow within the mantle is approximated by an exponentially decaying hydrostatic response function (that is, the mantle is treated as a viscous half-space).

[53] Each of the three nontrivial models is described in turn below. An earth model is formulated by combining one of the lithosphere models with one of the mantle approximations. Glimmer therefore implements four different simple Earth models referred to as local lithosphere/fluid asthenosphere (LLFA), local lithosphere/relaxing asthenosphere (LLRA), elastic lithosphere/fluid asthenosphere (ELFA) and elastic lithosphere/relaxing asthenosphere (ELRA).

4.1. Local Lithosphere

[54] Since there are no lithospheric effects, the equilibrium bedrock depression h_d can be found from the ice thickness H according to Archimedes' Principle

$$h_d = \frac{\rho_i}{\rho_{\text{ast}}} H, \tag{67}$$

where ρ_i is the density of ice and ρ_{ast} is the effective density of the asthenosphere (values given in Table 1).

4.2. Elastic Lithosphere

[55] The local lithosphere approximation can be improved by introducing a thin elastic plate resting on the asthenosphere. The additional elastic layer only affects the geometry of the deformation.

[56] The downward deflection $h_d(r)$, due to a load q, of a thin elastic plate with thickness H_L and flexural rigidity D floating on a nonviscous medium with density ρ_{ast} can be written as [*Lambeck and Nakiboglu*, 1980; *Le Meur and Huybrechts*, 1996]

$$D \nabla^4 h_d + \rho_{\text{ast}} g h_d = q, \tag{68}$$

where ∇ is the horizontal gradient operator and g is the gravitational acceleration. The flexural rigidity in terms of the Lamé parameters, λ and μ, and the plate thickness is [*Lambeck and Nakiboglu*, 1980]

$$D = \frac{\mu(\lambda + \mu) H_L^3}{3(\lambda + 2\mu)}. \tag{69}$$

[57] For a radially symmetric load of finite dimension with boundary at $r = B$, with r being the radial dimension in a polar coordinate system, the boundary conditions to the 4th-order differential equation (68) are [*Lambeck and Nakiboglu*, 1980]: (1) h_d and dh_d/dr are finite at $r = 0$, (2) h_d and dh_d/dr are continuous at $r = B$, (3) moments and

shears are continuous at $r = B$, and (4) moments vanish at infinity: h_d and $r^{-1}/(dh_d/dr)$ vanish at infinity.

[58] Solutions of (68) for a uniform disk load of density ρ_i, height H and radius A are, for $r \leq A$

$$h_d(r) = \frac{\rho_i H}{\rho_{ast}} \left[1 + C_1 \mathrm{Ber}\left(\frac{r}{L_r}\right) + C_2 \mathrm{Bei}\left(\frac{r}{L_r}\right) \right], \quad (70)$$

and for $r \geq A$

$$h_d(r) = \frac{\rho_i H}{\rho_{ast}} \left[D_1 \mathrm{Ber}\left(\frac{r}{L_r}\right) + D_2 \mathrm{Bei}\left(\frac{r}{L_r}\right) + D_3 \mathrm{Ker}\left(\frac{r}{L_r}\right) + D_4 \mathrm{Kei}\left(\frac{r}{L_r}\right) \right], \quad (71)$$

where the functions Ber(x), Bei(x), Ker(x) and Kei(x) are zeroth-order Kelvin functions. $L_r = (D/(\rho_{ast} g))^{1/4}$ is the radius of relative stiffness. The constants C_i and D_i arise from the boundary conditions and can be written as

$$\begin{aligned} C_1 &= a\mathrm{Ker}'(a), \\ C_2 &= -a\mathrm{Kei}'(a), \\ D_1 &= 0, \\ D_2 &= 0, \\ D_3 &= a\mathrm{Ber}'(a), \\ D_4 &= -a\mathrm{Bei}'(a), \end{aligned} \quad (72)$$

where $a = A/L_r$ [*Lambeck and Nakiboglu*, 1980]. The prime denotes first derivatives, i.e., $f'(a) = \frac{df(x)}{dx}|_{x=a}$.

[59] The load imposed on the lithosphere by a column with a square base with edges Δx can be approximated by a number of disk loads, provided the volume and thus the mass is conserved. The maximum difference of a square load with a volume of 3 km $\times$ 400 km^2 approximated with 1 disk and 64 disks is about 5 cm or 0.0017% [*Hagdorn*, 2008]. The ice load with a rectilinear base is therefore approximated using a single cylinder containing the same volume of ice.

4.3. Relaxing Asthenosphere

[60] The simplest way to account for the time dependence of the isostatic response is to estimate its characteristic time constant τ_{ast} and assume that the rate of response is proportional to the difference between the loaded equilibrium, $h_0 - h_d$, and the current profile, h, and inversely proportional to the time constant [*Le Meur and Huybrechts*, 1996]. The rate of isostatic adjustment is then

$$\frac{dh}{dt} = -\frac{1}{\tau_{ast}} (h - h_0 + h_d). \quad (73)$$

In glaciated regions, the present-day depression of the topography is assumed to be in equilibrium with the ice load, allowing the equilibrium unloaded topography to be calculated. In ice-free regions, the present-day topography is assumed to be the equilibrium unloaded topography. However, these assumptions are crude estimates because isostatic adjustment time scales are so long: glacial rebound is still ongoing in many formerly glaciated regions, e.g., present uplift rates over the Gulf of Bothnia are about 12 mm a^{-1} [*Milne et al.*, 2001]. Note that equation (73) does not take into account contributions from changes in sea level, although the method could be adapted to do so.

5. Software Design Considerations

5.1. Standards Compliance

[61] In implementing Glimmer, adherence to widely used standards has been a priority, in order to aid the widespread use of the model. The most significant such standards concern the code itself, and the form of the model data input and output. Consequently, all model code in Glimmer adheres to the FORTRAN 95 standard (explained by *Metcalf and Reid* [1999]). Compiler- and platform-dependent features are not used. The model uses the NetCDF file format [*Rew and Davis*, 1990], and adheres to the Climate and Forecast metadata standard 1.0 (CF: http://www.cfconventions.org/) for all input and output files.

5.2. Multiple Instances

[62] Two of the most important characteristics of ice sheets are that they are regional features, and that they are affected by processes that occur on small spatial scales, such as marginal ablation. These properties lead naturally to the formulation of ice sheet models on regional rather than global grids, since they offer the high-resolution coverage needed, without the computational cost that would otherwise be incurred. This is the approach adopted by most such models [e.g., *Huybrechts*, 1986; *Huybrechts et al.*, 1996], and is that taken by Glimmer as well.

[63] When only a single region is being modeled (for instance, Greenland or Antarctica), the regional high-resolution approach is not a limitation, but where more than one ice sheet is of interest, especially as part of a coupled climate–ice sheet system, the regional formulation of the ice model can be problematic. The reason for this is that most model codes only allow one copy of each model field array to be held at a time: either Greenland or Antarctica can be modeled, but not both. Historically, FORTRAN, which is the most common language for scientific computing, has not allowed the wholesale duplication of a model's variables and arrays in a simple fashion. One approach to this difficulty is to use a global domain for the ice sheet model [e.g., *Pollard and Thompson*, 1997], but this is computationally wasteful. Alternatively, an extra dimension could be added to all model arrays, an ice sheet index, but this is complex to implement, and requires that each ice sheet domain have the same number of grid points in a given direction.

[64] Glimmer makes use of derived types, a feature of more recent FORTRAN standards (FORTRAN 90 and 95, abbreviated to f90/95), to overcome this difficulty. Derived types are a way of packaging a collection of variables and arrays to form a new data type, similar to a class or structure in some other languages. Derived types may be nested within one another, and arrays of a derived type may be declared. In Glimmer, all the model field arrays and other data necessary for the calculation are contained in a set of nested derived types. Only the most universal data (some constants and scaling parameters) are contained in f90/95 modules (similar to COMMON blocks in previous versions of FORTRAN). In addition, all Glimmer model subroutines are stateless (they do not retain any data from one call to the

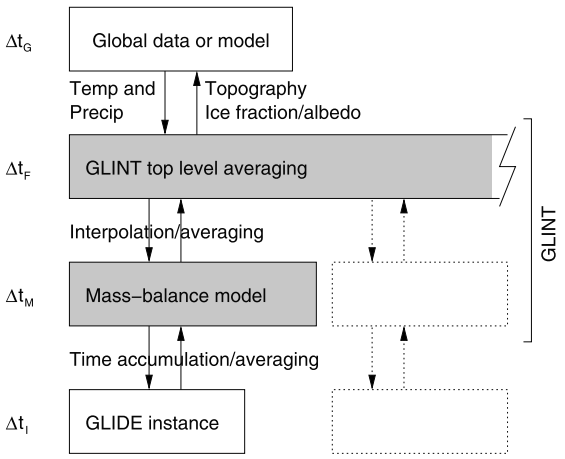

Figure 2. Structure of GLINT (shaded) in relation to GLIDE and global forcing data. Information flow is indicated by arrows. Dotted lines denote an additional GLIDE instance and associated mass balance model; an arbitrary number of these may be configured. Four time steps are used, such that $\Delta t_G \leq \Delta t_F \leq \Delta t_M \leq \Delta t_I$; these are explained in the text.

next) because all data are contained in derived types, and passed in through the parameter list.

[65] Since all necessary data are described in the definitions of the relevant derived types, any number of instances of these derived types may be declared, corresponding to an arbitrary number of ice sheet models. Integrating an ice sheet model forward one time step is then accomplished by passing the relevant instance of the model variable type to the appropriate subroutine. For convenience, an array of ice sheet models may be declared, and stepped forward in turn using a do loop.

5.3. Automatic Restart Code

[66] When doing long model integrations, and especially when using time-shared high-performance computing resources, it is convenient to be able to dump the complete state of a model to file at a given point. The model run may then be restarted from the same point at a later date. While many numerical models of the atmosphere and other climate system components include such a capability, it is time consuming to write and maintain code to handle restarts. Every time a variable or array is changed in the model, the restart code needs to be updated as well. In a complex model such as Glimmer, the need to maintain consistency between the restart code and the rest of the model provides too many opportunities for coding errors, and increases the personnel resources needed to maintain the model as new features are added.

[67] To overcome this difficulty, an automatic method for generating restart code is included in Glimmer. A program that parses f90/95 code (i.e., analyzes its structure and interprets the meaning of each element of the code) has been implemented in the object-orientated language Python. This is applied to each of the Glimmer source files in turn. For each module variable or derived type, a set of subroutines is generated to read and write the model data to a NetCDF-format file. Nested derived types and pointer arrays are all handled automatically, and the resulting code allows the model state to be written to file using a single subroutine call. Furthermore, because the restart file conforms to the NetCDF standard, it can be viewed with a range of widely available software, which is useful for debugging and analysis.

6. Coupling to the Global Climate: GLINT Module

[68] The interaction between ice sheets and the global climate is of great importance and interest. It is of contemporary importance in respect of climate change, and the possible future sea level rise attributed to the melting of ice sheets; in addition, the feedbacks between ice sheets and the climate system have also been implicated in longer-term glacial cycles [see, e.g., *Vettoretti and Peltier*, 2004]. The need to couple ice sheet models to climate models is the natural result of this.

[69] As noted in section 1.2 above, Glimmer has a modular structure which is designed to allow the climatic forcing to be specified flexibly, through the use of different climate drivers. The simplest such drivers are of the type used for the benchmarking experiments described in section 7 below. To simulate the evolution of an ice sheet within the global climate system requires a much more complex climate driver, one that can process the output from the other model components into a form appropriate for the ice sheet, as well as returning relevant fields from the ice sheet to the atmosphere. The central difficulty is that the temporal and spatial scales relevant to atmospheric evolution (hours and hundreds of km) are markedly different from those important for the ice sheet (decades and tens of km). The Glimmer Interface (GLINT) coupling module, provided as part of Glimmer, addresses this problem.

6.1. Design and Structure

[70] GLINT was developed as part of the GENIE Earth System model [*Lenton et al.*, 2007], to enable interactive coupling between Glimmer and the other components of the model; however, the design of GLINT is intended to make it straightforward to use with other climate models, or with "off-line" sources of global climate data such as reanalysis data sets.

[71] Figure 2 shows the general structure of GLINT as it relates to the core ice model (GLIDE) and to the global forcing data. Instantaneous surface air temperature and precipitation data is available at intervals Δt_G (the global time step), which is either the climate model time step or the data interval, depending on whether GLINT is coupled interactively to a climate model or is being forced off-line with data. These are passed to the top level GLINT code at intervals of Δt_F (the forcing time step), which may be greater than or equal to Δt_G.

[72] The main GLINT code accumulates the input fields over the length of the mass balance time step (Δt_M), and then transforms the data onto the ice sheet model grid. The mass balance calculations are finally accumulated over the length of the GLIDE time step (Δt_I), before being passed to the ice sheet model. Fractional ice and snow cover, albedo,

and surface topographic elevation are passed back from GLIDE and transformed onto the global grid to be supplied back to the global model if necessary. In addition, the domain-integrated input and output water fluxes are available to the global model at each ice sheet time step.

[73] As Figure 2 indicates, an arbitrary number of ice sheet model instances may be coupled to a global climate model using GLINT. The coordination of the separate instances is handled automatically by GLINT.

6.2. Spatial Transformation of Data

[74] GLINT assumes that the global climate model or reanalysis data is defined on a latitude-longitude grid (the "Global" grid), which may have uneven spacing in latitude (to allow for Gaussian/spectral grids). However, the ice sheet model is defined on a rectangular Cartesian grid (x-y, termed the "Local" grid). For the purposes of GLINT coupling, a map projection is defined for the Glimmer grid, as this is used to transform data from one grid to the other. A key component of GLINT performs this transformation.

6.2.1. Spatial Transformation: Global to Local

[75] In transforming forcing data from the global grid to the local grid, the conservation of mass and energy between the two grids is of particular importance. Two things make this a nontrivial problem: first, the two grids are not generally aligned with one another, and their relative angle and resolution varies spatially. Second, because of numerical stability considerations, Glimmer requires input fields that vary smoothly over the ice sheet domain.

[76] Because the two grids are not coincident, and to obtain a smooth field, data from the global grid needs to be interpolated onto the ice sheet grid. Nevertheless, this raises difficulties because the data on the global grid are generally considered to represent the mean value for each grid box, rather than point values: it is debatable whether this is an appropriate assumption for finite difference models, but it remains the most practical and widely used interpretation. For many interpolation schemes (for example, bilinear interpolation), it is not necessarily true that the integral of a given field on the ice sheet grid will equal the integral over the same region on the global grid.

[77] To overcome this problem, it is necessary to use an interpolation scheme which preserves the mean of the global grid box on the Glimmer grid, while still delivering a smooth field to Glimmer. The method used is an adaption of bilinear interpolation and is termed "mean-preserving interpolation"; it fulfills the need to conserve quantities when transforming them onto the Glimmer grid.

[78] The data on the global latitude-longitude grid are denoted $\{\eta_{kl}\}$, where (k, l) is the index of a single grid point. Mean-preserving interpolation works by calculating a new set of gridded data $\{\eta'_{kl}\}$ which may then be bilinearly interpolated to an arbitrary intermediate point $\eta'_{\theta\phi}$. Here, (θ, ϕ) denotes the position in the global spherical coordinate system. To ensure that the mean of the interpolated field over the global grid box is the same as the value of η_{kl} at that point, the following constraint is applied

$$\int_{\theta_{k-\frac{1}{2}}}^{\theta_{k+\frac{1}{2}}} \int_{\phi_{l-\frac{1}{2}}}^{\phi_{l+\frac{1}{2}}} \eta'_{\theta\phi} \cos\phi \, d\theta d\phi = \eta_{kl} \int_{\theta_{k-\frac{1}{2}}}^{\theta_{k+\frac{1}{2}}} \int_{\phi_{l-\frac{1}{2}}}^{\phi_{l+\frac{1}{2}}} \cos\phi \, d\theta d\phi. \quad (74)$$

Because $\eta'_{\theta\phi}$ can be expressed as a linear combination of the nearest four points in the interpolant field $\{\eta'_{kl}\}$ (by bilinear interpolation), the integrals in (74) can be evaluated analytically, which yields a sparse matrix equation giving $\{\eta'_{kl}\}$ in terms of $\{\eta_{kl}\}$. This is solved using the SLAP Library also employed elsewhere in the model [*Seager*, 1988]. Because the geometry of the problem does not change as the model run progresses, the elements of the sparse matrix only need to be calculated at the beginning of the integration.

6.2.2. Spatial Transformation: Local to Global

[79] Transformation of data from the ice sheet model grid to the global grid is accomplished by areal averaging, such that the value on the global grid is the mean of the points contained within it on the ice sheet model grid

$$\eta_{kl} = \sum \eta_{ij}, \quad (75)$$

where the sum is made over the points on the Glimmer grid $\{x_{ij}, y_{ij}\}$ which are contained within the global grid box (k, l).

[80] This method is only approximately conservative, although its conservation properties improve as the number of Glimmer grid points contained in each global grid box increases. The lack of strict conservation in this method is caused by the nontrivial intersection between the two grids. Some Glimmer grid boxes intersect with more than one global grid box, but calculating the exact partitioning between these is complex. Strict conservation is not essential in the transformation of quantities such as topographic elevation and albedo from the ice sheet to the global model, so the areal averaging scheme used is considered adequate for this task. If a more realistic surface model were to be added to GLINT, such that mass and energy fluxes (e.g., evaporation) were being returned to the global model, a strictly conservative aggregation model would be necessary.

6.3. Mass Balance Schemes

[81] Two mass balance models are implemented within GLINT, both of which are based on the positive degree day (PDD) method. One model calculates an annual mass balance, while the other does so on a daily basis; they are described in the following sections. The principle of the PDD approach is that the energy available for melt is proportional to the time integral of temperature above 0°C, so that

$$\text{Melt} = \alpha \int_{t_0}^{t_1} \max(T_a, 0) = \alpha D_p dt. \quad (76)$$

The constant α is known as the "PDD factor," and D_p is the number of positive degree days in the given period. In both models described here, different PDD factors are used for snow (α_s) and ice (α_i), to account for the differences in albedo between the two materials. The default values of the parameters used in both models are given in Table 2.

6.3.1. Annual PDD Model

[82] The annual PDD scheme is an implementation of the model described by *Reeh* [1991]. It is based on the assumption that the annual cycle of temperature $T_a(t)$ at

Table 2. List of Parameters Used in the Two PDD Models and Their Default Values[a]

Symbol	Description	Value	Units
α_s	PDD factor for snow	0.003	m water d^{-1} °C^{-1}
α_i	PDD factor for ice	0.008	m water d^{-1} °C^{-1}
σ_T	standard deviation of temperature fluctuations	5.0	°C
$w_{\max}$	fraction of snowfall that can refreeze	0.6	
T_R	temperature threshold for partitioning precipitation into rain and snow	1.0	°C
ρ_s	density of fresh snow	300	kg m^{-3}
β_F	density of firn-ice boundary as a fraction of the density of ice ρ_i	0.872	
C	exponential factor in snow density profile	0.0165	m^{-1}
λ_{firn}	time scale for firn compaction	10	years

[a]Note that not all parameters are used in both models, but those that are have the same default values in each case.

each grid point is sinusoidal, with an additional random variation to account for diurnal and other fluctuations

$$T_a(t) = \overline{T}_a - \Delta T_a \cos\left(\frac{2\pi t}{A}\right) + \mathbf{R}(0, \sigma_T), \tag{77}$$

where $\overline{T}_a$ is the mean annual air temperature, ΔT_a is the annual air temperature half range, A is the period of a year, and $\mathbf{R}(0, \sigma_T)$ is a random fluctuation drawn from a normal distribution with mean 0°C and standard deviation σ_T.

[83] The number of positive degree days in a year for this temperature series is given by

$$D_p = \frac{1}{\sigma_T\sqrt{2\pi}} \int_0^A \int_0^\infty \overline{T}_a \exp\left(\frac{-\left(\overline{T}_a - T_a\right)^2}{2\sigma_T^2}\right) dT dt. \tag{78}$$

In practice, the inner integral (dT) is evaluated between 0 and $T_a + 2.5\sigma_T$. For computational efficiency, (78) is evaluated using Romberg integration [*Bauer*, 1961] for a range of values of $\overline{T}_a$ and ΔT_a when the model is initialized, and these values are stored in a look-up table. The final value of D_p is determined using bilinear interpolation from the four entries in the table nearest to the actual values of $\overline{T}_a$ and ΔT_a.

[84] Because different PDD factors are used for ice and snow, it is necessary to include a simple representation of meltwater refreezing within the firn layer, again following the method of *Reeh* [1991]. In this model, the firn layer is assumed to compact to ice in the course of the year, which means there is no need to keep track of firn properties from year to year.

[85] In this model, all precipitation is assumed to fall as snow. The starting point for the firn model is therefore a depth of snow equal to the annual precipitation P, which is conventionally given as a water-equivalent depth. Applying (76), the potential snow melt $\hat{a}_s = \alpha_s D_p$. Here, and in the following discussion, the hat indicates a snow or ice thickness given as a water-equivalent depth. The capacity of the snowpack to hold meltwater by refreezing $\hat{b}_0$ is given by

$$\hat{b}_0 = w_{\max} P, \tag{79}$$

where $w_{\max}$ is a parameter. The potential amount of snow ablation is compared with the ability of the snow layer to absorb the melt. Three cases are possible. First, all snowmelt is held within the snowpack and no runoff occurs ($\hat{a} = 0$). Second, the ability of the snowpack to hold meltwater is exceeded but the potential snow ablation is still less than the total amount of precipitation so that $\hat{a} = \hat{a}_s - \hat{b}_0$. Finally, the potential snowmelt is greater than the precipitation (amount of snow available), so that ice melt ($\hat{a}_i$) has to be considered as well. In this final case, the total ablation is the sum of snowmelt (total precipitation minus meltwater held in refreezing) and ice melt (calculated by deducting from the total number of degree days the number of degree days needed to melt all snowfall, converted to an amount of ice melt)

$$\hat{a} = \hat{a}_s + \hat{a}_i = P - \hat{b}_0 + \alpha_i\left(D_p - \frac{P}{\alpha_s}\right). \tag{80}$$

This leaves the total annual ablation $\hat{a}$; the total net mass balance is given by the difference between the total annual precipitation and the total annual ablation.

6.3.2. Daily PDD Model

[86] The daily PDD model is based on the same principles as the annual scheme, except that the diurnal variations are resolved explicitly. A significant advantage of this model over the annual PDD model is that the seasonal cycle of snow depth can be simulated. In this model, the mass balance is calculated each day, and a simple firn model is used to keep track of the variations in the amount of snow and superimposed ice.

[87] The diurnal variation $T_d(t)$ is assumed to be sinusoidal, so that

$$T_d(t) = \overline{T}_d - \Delta T_d \cos\left(\frac{2\pi t}{t_d}\right), \tag{81}$$

where t_d is the length of a day. This means that the number of positive degree days D_p for a single day is given by

$$D_p = \int_0^{t_d} \max\left[\overline{T}_d - \Delta T_d \cos\left(\frac{2\pi t}{t_d}\right), 0\right] dt. \tag{82}$$

This integral may be evaluated analytically to give

$$D_p = \begin{cases} \overline{T}_d & \text{if } \left(\overline{T}_d - \Delta T_d\right) \geq 0 \\ 0 & \text{if } \left(\overline{T}_d + \Delta T_d\right) < 0 \\ \frac{1}{\pi}\left(\overline{T}_d(\pi - \theta_0) + \Delta T_d \sin\theta_0\right) & \text{otherwise} \end{cases}, \tag{83}$$

where $\theta_0 = \cos^{-1}(\overline{T}_d/\Delta\ T)$, the time at which $T_d = 0$.

[88] Precipitation is partitioned into rain and snowfall depending on a temperature threshold T_R, with precipitation falling as rain when $T_d > T_R$, and as snow otherwise. This leads to

$$P_R = \begin{cases} P & \text{if } \left(\overline{T}_d - \Delta T\right) > T_R \\ 0 & \text{if } \left(\overline{T}_d + \Delta T\right) < T_R \\ P\left[1 - \frac{1}{\pi}\cos^{-1}\left(\frac{\left(\overline{T}_d - T_R\right)}{\Delta T}\right)\right] & \text{otherwise} \end{cases}, \quad (84)$$

with $P = P_S + P_R$, and P_R and P_S being the quantities of rain and snow, respectively. As with the annual PDD model, precipitation is given as a water-equivalent depth in these calculations, and different PDD factors are used for snow and ice: α_s and α_i, respectively.

[89] The values of D_p, P_R and P_S are used to drive a simple model of firn evolution and snow densification. The firn model is based on the same methods used in the annual PDD model. In the following description, the water-equivalent depths of snow and superimposed ice at the beginning of the day are denoted $\hat{h}_{s,n}$ and $\hat{h}_{i,n}$, respectively. The subscript n denotes the value at the start of the time step, and the hats denote water-equivalent depths. The depths of snow and superimposed ice are together taken as the depth of the firn layer: $\hat{h}_n = \hat{h}_{s,n} + \hat{h}_{i,n}$. As with the annual PDD model, it is assumed that runoff will occur only when superimposed ice comprises greater than a prescribed fraction $w_{\max}$ of the total firn depth, because of the fact that meltwater will first percolate into the firn layer. The runoff threshold $\hat{b}_0$ is given by

$$\hat{b}_0 = w_{\max}\left(P + \hat{h}_n\right). \quad (85)$$

It is assumed that liquid precipitation P_R freezes as superimposed ice, and that snowmelt refreezes as superimposed ice while $\hat{h}_n \leq \hat{b}_0$.

[90] As before, the potential ablation of snow is given by

$$\hat{a}_s = \alpha_s D_p. \quad (86)$$

[91] If there is insufficient snowmelt for runoff to occur (when $\hat{a}_s + \hat{h}_{i,n} + P_R \leq \hat{b}_0$), then the new values for snow and superimposed ice depth are as follows

$$\hat{h}_{s,n+1} = \hat{h}_{s,n} + P_S - \hat{a}_s, \quad (87)$$

$$\hat{h}_{i,n+1} = \hat{h}_{i,n} + P_R + \hat{a}_s. \quad (88)$$

[92] If this limit is exceeded, the level of superimposed ice is topped up to the level of $\hat{b}_0$, and the amount of snow to be ablated is reduced accordingly

$$\hat{a}_s = \alpha_s D_p - \left(\hat{b}_0 - \hat{h}_{i,n}\right). \quad (89)$$

[93] There will not always be sufficient snow available to realize the potential ablation (i.e., if $\hat{a}_s > \hat{h}_{s,n}$); in this case, the potential ablation remaining after all the snow has been melted is converted to potential ablation of ice

$$\hat{a}_i = \frac{\alpha_i}{\alpha_s}\left(\hat{a}_s - \hat{h}_{s,n}\right), \quad (90)$$

$$\hat{h}_{s,n+1} = 0. \quad (91)$$

This potential ablation is subtracted from the amount of superimposed ice, which generates runoff. If the potential ablation of ice is greater than the amount of superimposed ice, the residual is ablated from glacial ice, also as runoff.

6.3.3. Snow Densification Model

[94] By itself, the daily PDD model provides no mechanism for the conversion of firn into glacial ice by densification, meaning that the modeled firn depth will be equal to the net mass balance since the beginning of the run. This is clearly unreasonable over long time periods, and so the conversion of firn into glacial ice is parameterized within the model. The physical processes involved in this conversion are complex, and depend on the local climate. However, they may be broadly represented by two mechanisms: the refreezing of melt to form superimposed ice, and the pressure compaction of snow (known as sintering). The first of these is represented in the PDD scheme, so it is the second which is addressed here.

[95] Because firn is only represented in the daily PDD model by a single homogeneous layer ($\hat{h} = \hat{h}_s + \hat{h}_i$), no information is held regarding either the age or the density of the material. Thus, while the process we are trying to parameterize is strictly firn densification, it will be represented by a time-dependent reduction in $\hat{h}_s$ and $\hat{h}_i$.

[96] *Paterson* [1994] gives an empirical relationship between density ρ and depth z_d in an ice mass, being an exponential approach toward the density of ice ρ_{i}

$$\rho = \rho_{\mathrm{i}} - (\rho_{\mathrm{i}} - \rho_{\mathrm{s}})\exp(-Cz_d), \quad (92)$$

with ρ_{s} being the density of snow at the surface (i.e., freshly fallen snow), and C is a parameter, determined from field measurements.

[97] To model the densification of snow in our single-layer model, we make a number of assumptions: (1) The equilibrium density profile of the snow in the firn layer is given by (92), (2) the superimposed ice has constant density ρ_{i}, (3) the relative volume fractions of ice and snow are the same throughout the firn layer, and (4) the boundary between firn and glacial ice occurs when the density of the firn is some fraction β_F of the density of ice ρ_{i}.

[98] The aim is to determine the equilibrium depth of the firn layer (as a water-equivalent depth), given a particular composition of snow and superimposed ice. The actual depth in the model is then relaxed toward this value according to a given time constant.

[99] The total amount of firn in the layer is $\hat{h}_s + \hat{h}_i$, so that the relative fractions of snow (β_s) and superimposed ice (β_i) in the layer are as follows

$$\beta_s = \frac{\hat{h}_s}{\hat{h}_s + \hat{h}_i}, \tag{93}$$

$$\beta_i = \frac{\hat{h}_i}{\hat{h}_s + \hat{h}_i}. \tag{94}$$

The density profile ρ_F of the combined firn layer is a weighted mean of the densities of the snow and ice separately

$$\rho_F = \rho_\mathrm{i} - \beta_s(\rho_\mathrm{i} - \rho_\mathrm{s}) \exp(-C z_d). \tag{95}$$

The transformation from actual depth z_d to water-equivalent depth $\hat{z}_d$ is achieved using

$$d\hat{z}_d = \frac{\rho_F}{\rho_\mathrm{w}} dz_d, \tag{96}$$

where ρ_w is the density of water. By applying (96) to (95), and integrating between 0 and a given depth, we find that

$$\hat{z}_d = \frac{1}{\rho_\mathrm{w}} \left[\rho_\mathrm{i} z_d + \frac{\beta_s(\rho_\mathrm{i} - \rho_\mathrm{s})}{C} (\exp(-C z_d) - 1) \right]. \tag{97}$$

Rearranging (95) gives

$$z_d = \frac{1}{C} \ln\left[\frac{\beta_s(\rho_\mathrm{i} - \rho_\mathrm{s})}{\rho_\mathrm{i} - \rho_F} \right], \tag{98}$$

which can be combined with (97) to give $\hat{z}_d$ in terms of ρ_F

$$\hat{z}_d = \frac{1}{C\rho_\mathrm{w}} \left\{ \rho_\mathrm{i} \ln\left[\frac{\beta_s(\rho_\mathrm{i} - \rho_\mathrm{s})}{\rho_\mathrm{i} - \rho_F} \right] + \beta_i \rho_\mathrm{i} + \beta_s \rho_\mathrm{s} - \rho_F \right\}. \tag{99}$$

The boundary of firn and ice is the point where $\rho_F = \beta_F \rho_\mathrm{i}$, and so the equilibrium thickness of the firn layer as a water equivalent depth ($\hat{z}_{d0}$) is given by

$$\hat{z}_{d0} = \frac{1}{C\rho_\mathrm{w}} \left\{ \rho_\mathrm{i} \ln\left[\frac{\beta_s(\rho_\mathrm{i} - \rho_\mathrm{s})}{\rho_\mathrm{i}(1 - \beta_F)} \right] + (\beta_i - \beta_F)\rho_\mathrm{i} + \beta_s \rho_\mathrm{s} \right\}. \tag{100}$$

Having determined the equilibrium depth of firn for given relative fractions of snow and ice, the two component depths are relaxed toward it, such that their respective fractions of the firn layer remain constant

$$\frac{d\hat{h}_i}{dt} = \frac{\beta_i \hat{z}_{d0} - \hat{h}_i}{\lambda_\mathrm{firn}}, \tag{101}$$

$$\frac{d\hat{h}_s}{dt} = \frac{\beta_s \hat{z}_{d0} - \hat{h}_s}{\lambda_\mathrm{firn}}, \tag{102}$$

for $\hat{z}_d > \hat{z}_{d0}$, with $d\hat{h}/dt = 0$ otherwise. The time scale for firn densification λ_firn is a tunable parameter.

[100] *Paterson* [1994] provides values of C and other data for six sites in Greenland and Antarctica. Of these, the data for Dome C are most likely to represent a column of dry snow with an equilibrium density profile, since it is by far the coldest site of those given, and also has the lowest annual accumulation. For Dome C, *Paterson* [1994] has $C = 0.0165\ \mathrm{m}^{-1}$, based on *Alley et al.* [1982]. This is significantly smaller than for the other sites, whose values range between $0.0235\ \mathrm{m}^{-1}$ and $0.0314\ \mathrm{m}^{-1}$. This difference could be interpreted as supporting the view that Dome C most resembles the pure snow column, since it is reasonable to expect density to increase more quickly with depth in the presence of superimposed ice. Together with the depth of the firn-ice boundary (100 m) given by *Paterson* [1994], it can be inferred from this value, using (92), that $\beta_F = 0.872$. Other constants in (100) are well known; all these are given in Table 2.

6.3.4. Forcing Field Downscaling

[101] As explained, the spatial scales that are important in ice sheet modeling are smaller than those represented in climate models. Ice sheet mass balance depends on the sum of surface processes of accumulation and ablation that vary substantially over short distances, because of differences in the local climate. The global climate forcing supplied to GLINT will most frequently not have high enough resolution to capture these variations, and it is advantageous to apply some kind of "downscaling" process after it has been transformed onto the Glimmer grid.

[102] The downscaling of temperature is commonly achieved by a correction to account for difference in altitude between the low-resolution topography of the climate model (s_G) and the high-resolution topography of the ice sheet model [e.g., *Pollard and Thompson*, 1997]. The correction factor is the vertical lapse rate L_G, which yields the corrected temperature T'_a

$$T'_a = T_a + L_G(s_G - s). \tag{103}$$

The default value of L_G is given in Table 1. Precipitation downscaling is more problematic, and is not implemented in GLINT: the interpolated large-scale precipitation field is used instead.

6.3.5. Temporal Analysis of Temperature Data

[103] Both the daily and annual PDD models of mass balance take as input the mean and half-range of the surface air temperature over their respective time steps. In both cases, what is needed is the half-range of a sine wave fitted through the input data. This is particularly true for the annual model, where the diurnal and other variability is accounted for in the stochastic term.

[104] Typically, the global climate data used to drive GLINT is available at 6-hourly intervals or more frequently. The most efficient way to fit a sine wave through this data is by evaluating the first nonzero frequency term in a Fourier series representation of the data

$$\Delta T_a = \frac{2}{N} \left| \sum_{k=0}^{N-1} T_k \exp\left(i \frac{2\pi k}{N} \right) \right|, \tag{104}$$

where N is the number of time slices per mass balance time step, T_k is the value of the temperature at time t_k, and, in

Table 3. Ice Divide Thicknesses Simulated by Glimmer, Compared With EISMINT-1 Results Reported by *Huybrechts et al.* [1996][a]

	EISMINT-1			Glimmer		
Experiment	All	Type I	Type II	ADI	Linear	Nonlinear
Fixed margin A	3384.4 ± 39.4	3419.9 ± 1.7	3342.6 ± 0.4	3427.44	3424.70	3424.70
Fixed margin B	3230.1 ± 34.8	3264.8 ± 5.6	3195.3 ± 2.6	3272.04	3269.33	3269.12
Fixed margin C	3306.6 ± 35.9	3341.7 ± 3.9	3271.4 ± 3.2	3350.31	3347.44	3347.19
Moving margin A	2978.0 ± 19.3	2997.5 ± 7.4	2958.9 ± 1.3	2992.19	2989.17	2989.17
Moving margin B	2794.2 ± 20.0	2813.5 ± 2.0	2775.7 ± 10.6	2810.63	2807.58	2807.36
Moving margin C	2859.2 ± 19.2	2872.5 ± 6.8	2846.0 ± 18.6	2876.77	2874.05	2873.79

[a]Different experiment labels refer to steady state forcing (A) and sinusoidal forcing with period 20 ka (B) or 40 ka (C). Unit is m.

(104) only, $i = \sqrt{-1}$. For this to be possible, N must be even. Because N is known at the outset of the run, the exponential terms in (104) may be calculated beforehand.

7. Model Benchmarks

[105] Glimmer is a complex numerical model, and, as such, it is necessary to verify it against benchmark solutions in order to have confidence in its output. This section describes the testing of Glimmer against the EISMINT benchmarks [*Huybrechts et al.*, 1996; *Payne et al.*, 2000], referred to as EISMINT-1 and EISMINT-2, respectively, and against the analytical solutions for isothermal ice sheets prepared by *Bueler et al.* [2005]. All these benchmarks are formulated on idealized rectangular domains.

[106] The tests used are the best available for ice sheet models; nevertheless, it should be noted that they do not test every part of the model described in the preceding sections.

7.1. EISMINT-1 Benchmarks

[107] The intercomparison experiments of EISMINT-1 focus on the mechanical part of the model. Calculated temperatures are used as a diagnostic tool and are not coupled to ice flow, so that the flow law parameter A in equation (5) is taken to be a temperature-independent constant. Two different geometries are specified: fixed margin and moving margin. Different mass balance profiles are used to ensure that the margin of the ice sheet is at the edge of the domain in the former, but free to move within the domain in the latter. The reader is referred to *Huybrechts et al.* [1996] for a comprehensive description of the benchmark tests.

[108] The EISMINT-1 specification includes both steady state and time-dependent tests. The steady state experiment is referred to as ''A.'' The time-dependent tests have sinusoidally varying forcing, with a period of either 20 ka (B) or 40 ka (C).

[109] The final thicknesses at the ice divide simulated by Glimmer are shown in Table 3 for each numerical scheme (ADI, Linear, Nonlinear); the published results from *Huybrechts et al.* [1996] are also given. In all cases, the thicknesses simulated by Glimmer are greater than the mean values given in *Huybrechts et al.* [1996]. For the moving margin experiments, they lie within one standard deviation of the EISMINT mean, but, for the fixed margin experiments, they do not.

[110] *Huybrechts et al.* [1996] distinguish between two methods of discretizing the continuity equation (42), which they term type I and type II, and the results for the two groups of models separately are also given in Table 3. It might be expected that thicknesses calculated by Glimmer would closely match the results from one or other of these groups, but it can be seen from Table 3 that this is not the case. All the Glimmer results are closest to those for models of type I, but only a few lie within one standard deviation of the EISMINT-1 mean for that group. The reason for this is that the discretization used in Glimmer, although closer to type I than type II, is not strictly the same as either. This can be seen by comparing *Huybrechts et al.* [1996] with the model descriptions and results given in *Hindmarsh and Payne* [1996]. The latter paper gives three discretizations, termed methods 1, 2 and 3. Methods 2 and 3 correspond to EISMINT-1 types I and II, respectively, whereas Glimmer implements method 1. In their analysis, *Hindmarsh and Payne* [1996] concentrate on methods 2 and 3; the results from method 1 are expected to be more similar to method 2 than to method 3 because the size of the computational molecule is the same, despite there being more spatial averaging present in method 1 than in method 2.

[111] In the light of this, and in the absence of any published results for the EISMINT-1 experiments generated by a method 1 model, it is reasonable to conclude that the small differences between the Glimmer results and the published EISMINT-1 results are unlikely to be significant. As noted, the method 1 and method 2 discretizations are similar; particularly, the numerical diffusion they produce should be reasonably comparable, and consequently the thicknesses they produce should be similar, even if they are not identical.

[112] It should also be noted that the three numerical schemes implemented in Glimmer (ADI, Linear semi-

Table 4. Ice Divide Basal Temperatures Simulated by Glimmer, Compared With EISMINT-1 Results Reported by *Huybrechts et al.* [1996][a]

	EISMINT-1			Glimmer		
Experiment	All	Type I	Type II	ADI	Linear	Nonlinear
Fixed margin A	−8.97 ± 0.71	−8.84 ± 1.04	−9.04 ± 0.67	−8.93	−9.67	−9.67
Moving margin A	−13.34 ± 0.56	−13.43 ± 0.75	−13.29 ± 0.48	−13.41	−13.92	−13.92

[a]Only steady state experiment A shown. Unit is °C.

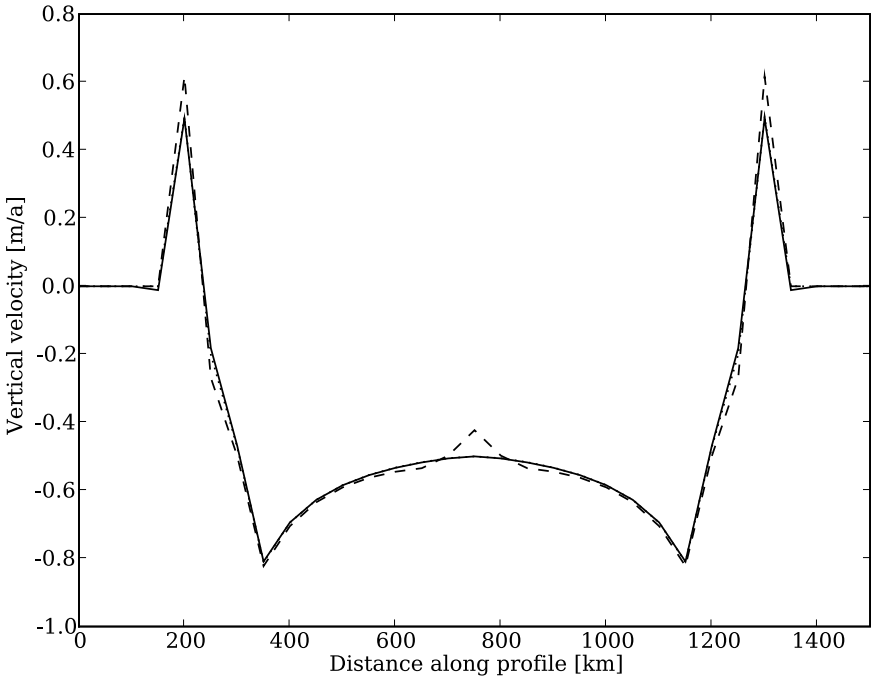

Figure 3. Vertical ice surface velocities of the moving margin EISMINT-1 experiment. The dashed line shows the uncorrected velocities; the dotted line shows the corrected velocities. The solid line shows the vertical velocity obtained from the upper kinematic boundary condition.

implicit, nonlinear) give results which are very close to one another. The differences between the three schemes are comparable to or smaller than the standard deviations of the type I model results given by *Huybrechts et al.* [1996]. This is further evidence that the equations in the model are being solved correctly, as the code used for the ADI scheme is substantially independent from that used for the linear and nonlinear semi-implicit schemes.

[113] Diagnostic basal temperatures at the ice divide for the steady state experiments compare well with those given by *Huybrechts et al.* [1996], and are shown in Table 4. Differences between the Glimmer results and those published by *Huybrechts et al.* [1996] are most likely to be due to differences in the ice thickness already discussed. A thicker ice sheet should yield a colder basal temperature, and this is the case here.

[114] As noted in section 2.7, there are circumstances where the vertical velocity does not match that determined by the kinematic upper boundary condition (15). This is illustrated by Figure 3, which shows a slice through the vertical velocities at the ice surface for the EISMINT-1 steady state moving margin experiment, compared with the vertical velocity obtained from the upper kinematic boundary condition. The slice shown is through the center of the domain: the vertical velocity obtained from (40) displays a spike at the exact center of the ice sheet, where none is present in the velocity obtained from the kinematic boundary condition. The reason for this difference is that the horizontal velocity is axially symmetric around this point. Because the horizontal velocity is calculated on the staggered (r, s) grid, the velocities used in the evaluation of (40) have directions which point NE, NW, SE and SW. However, to calculate the value of $\hat{\nabla} \cdot \mathbf{u}$ in (40), they are interpolated onto points lying directly north, east, south and west of the central point, so that

$$\left.\frac{\partial u}{\partial x}\right|_{i,j} = \frac{\left(u_{i+\frac{1}{2},j+\frac{1}{2}} + u_{i+\frac{1}{2},j-\frac{1}{2}}\right) - \left(u_{i-\frac{1}{2},j+\frac{1}{2}} + u_{i-\frac{1}{2},j-\frac{1}{2}}\right)}{2\Delta x}, \qquad (105)$$

with an equivalent expression for $\partial v/\partial y$.

Table 5. Brief Summary of EISMINT-2 Experiments Used in This Paper[a]

Experiment	Comment	Initial Condition
A	initial thermomechanical coupling run	zero ice
B	stepped 5 K air temperature warming	experiment A
C	stepped change in accumulation rate	experiment A
D	stepped change in equilibrium line altitude	experiment A
G	basal slip throughout	zero ice
H	basal slip only where basal ice is at melting point	zero ice

[a]Descriptions taken from *Payne et al.* [2000].

Table 6. Comparison Between EISMINT-2 Benchmarks and Glimmer Results: Ice Volume at End of Run[a]

	EISMINT-2	Glimmer
A	2.128 ± 0.051	2.112
B	**−2.589 ± 0.366%**	−2.079**%**
C	**−28.505 ± 0.369%**	−29.154**%**
D	−12.085 ± 0.324%	−12.166%
G	1.520 ± 0.014	1.519
H	1.900 ± 0.136	1.801

[a]Units are 10^6 km^3, except in experiments B, C, and D, where the result is expressed as a percentage difference from experiment A. Bold entries are those where the measured values fall outside one standard deviation of the reference measurements.

Table 7. Comparison Between EISMINT-2 Benchmarks and Glimmer Results: Ice Area at End of Run[a]

	EISMINT-2	Glimmer
A	1.034 ± 0.023	1.031
C	−19.515 ± 1.346%	−20.376%
D	−9.489 ± 1.267%	−10.188%
G	1.033 ± 0.021	1.026
H	1.032 ± 0.019	1.018

[a]Units are 10^6 km^2, except where percentage differences are given. Experiment B is omitted as the area remains constant compared with experiment A.

[115] As a consequence, the value of $\hat{\nabla} \cdot \mathbf{u}$ is a factor of $\sqrt{2}$ less than the correct value, which results in the vertical velocity at this point being incorrect by approximately the same factor. Constraining the vertical velocity to obey the upper kinematic boundary condition alleviates this problem (equation (41)). Note that this type of error is limited to places where there are large changes in the direction of flow over small horizontal distances, and it is unusual in numerical terms because it does not disappear as the spatial resolution is increased.

7.2. EISMINT-2 Benchmarks

[116] The EISMINT-2 model intercomparison [*Payne et al.*, 2000] concerns itself with thermomechanically coupled shallow ice models, as distinct from the uncoupled models which are the subject of EISMINT-1. Twelve experiments (A–L) are specified, of which six (A–D, G and H) are considered here. The main characteristics of each experiment are summarized in Table 5. Again, the reader is referred to *Payne et al.* [2000] for a full description of these tests.

[117] Tables 6–10 compare the output from Glimmer with the results published by *Payne et al.* [2000], for the five specified quantities (ice volume, ice area, fraction of base at or below melting point, ice thickness at the divide, and basal temperature at the divide). For comparability with the EISMINT-1 benchmarks, we have calculated the standard deviation of each benchmark from the data given by *Payne et al.* [2000], rather than use the total range. We have also discarded the results from model U in experiment G, which *Payne et al.* [2000] note is an outlier. Note also that in the case of experiments B, C and D, the quantities are given as differences compared to experiment A.

[118] The results from Glimmer mostly fall within one standard deviation of the mean values given by *Payne et al.* [2000]; those that do not are highlighted in bold in Tables 6–10. Identifying the reasons for the differences between the Glimmer results and those given by *Payne et al.* [2000] is difficult. Unlike *Huybrechts et al.* [1996] (EISMINT-1), the models evaluated by *Payne et al.* [2000] are not categorized by their horizontal discretization method (type I and type II). In addition, thermomechanical coupling introduces feedbacks between ice geometry, rheology and flow speed, making the effect of differences in discretization uncertain. It is notable that the results given by individual models given by *Payne et al.* [2000] display some variation in terms of their thermal configuration, evidenced by the shape of the part of the bed at pressure melting point. Consequently, it seems reasonable to conclude that the EISMINT-2 results given by Glimmer are still sufficiently close to the published values for these differences to be regarded as not of significance. Recently, a new set of exact solutions for thermomechanically coupled SIA models has been published [*Bueler et al.*, 2007]; testing Glimmer against these would be highly desirable, given the difficulty of interpreting the EISMINT-2 results unambiguously.

Table 8. Comparison Between EISMINT-2 Benchmarks and Glimmer Results: Area of Basal Melt as a Fraction of Total Area at End of Run[a]

	EISMINT-2	Glimmer
A	**0.718 ± 0.086**	0.808
B	11.836 ± 5.228%	7.808%
C	−27.806 ± 9.426%	−22.308%
D	−1.613 ± 1.784%	−1.362%
G	**0.305 ± 0.048**	0.215
H	0.529 ± 0.114	0.556

[a]Figures for experiments B, C, and D are percentage differences from experiment A. Bold entries are those where the measured values fall outside one standard deviation of the reference measurements.

Table 9. Comparison Between EISMINT-2 Benchmarks and Glimmer Results: Ice Divide Thickness at End of Run[a]

	EISMINT-2	Glimmer
A	**3688.342 ± 27.757**	3602.349
B	**−4.927 ± 0.394%**	−4.041%
C	−12.928 ± 0.405%	−12.807%
D	−2.181 ± 0.156%	−2.230%
G	2218.959 ± 5.205	2222.403
H	**3507.984 ± 118.086**	3343.324

[a]Units are meters, except in experiments B, C, and D, where the result is expressed as a percentage difference from experiment A. Bold entries are those where the measured values fall outside one standard deviation of the reference measurements.

[119] To give some indication of the speed of the model, we give sample model integration times, measured on a single core of an Intel Xeon 5140 processor (64 bit, 2.33GHz), with 4GB of RAM. The Intel Fortran compiler v.9.1, is used, and the operating system is 64-bit GNU/Linux. On this platform, the EISMINT-1 fixed margin experiment A is completed in approximately 76s, while EISMINT-2 experiment A is completed in approximately 412s. These timings are the means of timings from five model runs of each type.

7.3. Isothermal Exact Solutions

[120] *Bueler et al.* [2005] describe five analytical solutions to the isothermal shallow ice equations, denoted A to E. These solutions can be used to verify the numerical

Table 10. Comparison Between EISMINT-2 Benchmarks and Glimmer Results: Ice Divide Basal Temperature at End of Run[a]

	EISMINT-2	Glimmer
A	**255.605 ± 1.037**	254.439
B	4.623 ± 0.142	4.706
C	**3.707 ± 0.210**	3.939
D	−0.188 ± 0.019	−0.188
G	248.440 ± 0.591	248.286
H	**255.225 ± 1.056**	257.651

[a]Unit is K. In experiments B, C, and D, the result is expressed as a difference from experiment A. Bold entries are those where the measured values fall outside one standard deviation of the reference measurements.

Table 11. Time Step Lengths and Resolutions of Model Runs Used to Verify Glimmer Against the *Bueler et al.* [2005] Solutions

	Time Step (years)		
Horizontal Resolution (km)	ADI	Linear	Nonlinear
5.0	0.05	0.10	0.10
10.0	0.25	0.20	0.50
20.0	0.50	1.00	1.00
50.0	2.50	2.50	2.50

solution of the continuum equations. Benchmarks B, C and D use time-dependent mass balances and are considered here: Benchmark B is a similarity solution developed by *Halfar* [1983] with a moving natural margin, zero accumulation and constant volume; benchmark C is a similarity solution with rapid growth due to a positive time-dependent accumulation starting from zero ice thickness; and benchmark D is a solution with compensatory accumulation. Ice thickness oscillates in an annulus due to oscillating accumulation.

[121] Time-dependent behavior of an ice sheet model can then be verified using the exact solutions mentioned above, and described in detail in *Bueler et al.* [2005], by (1) using the exact ice thickness H at time $t = t_0$ as initial condition for the numerical model; (2) using the exact accumulation for each grid point at each time step; and (3) computing the errors between the numerical solution and the exact solution.

[122] In all three benchmarks, we verify the performance of Glimmer by calculating the thickness error at the center of the dome and the maximum thickness error across the domain, both for the final time step.

[123] The three benchmarks are run with the parameters taken from *Bueler et al.* [2005] for different grid spacings, Δx, summarized in Table 11. The time step Δt has to be reduced as the grid spacing is reduced to maintain stability of the numerical method. The ADI scheme is more unstable than the other schemes at small grid spacings, so its time steps have been reduced in comparison to theirs; even so, the ADI scheme was sufficiently unstable in benchmark D that it was impractical to shorten the time step enough to obtain results for grid spacings of 5 km and 20 km. In all cases, the minimum grid spacing was limited by computational expense: run times increase with decreasing grid spacing and time step size because the equations have to be solved at more nodes more often. Furthermore, the nonlinear solver takes about twice as long as the linear solver because of the additional Picard iterations.

[124] Figure 4 summarizes the results, giving the thickness error at the center of the dome, as well as the maximum thickness error, for all model runs. Figures 5 and 6 show the typical spatial distribution of errors.

[125] As expected, both the absolute error at the center of the ice dome and the maximum error generally decrease with decreasing grid spacing and time step size. The general trend is a clear convergence toward the analytical solutions, but there is some unevenness to the results as well. Not all increases in resolution result in reductions in errors. We propose two reasons for this variability: the effects of resolving the margin position, and the effect of insufficiently short time steps.

[126] First, the size of both the dome error and the maximum error will depend to some extent on the position of the margin. Because the margin is a discontinuity, its position is constrained by the grid spacing, so we expect the shape of the ice sheet to change unevenly as the grid spacing is changed. In addition, as *Hindmarsh and Payne* [1996] note, because of the discontinuity at the margin, the discretization used in Glimmer is known to be less than second-order accurate there. Figures 5 and 6 show that the

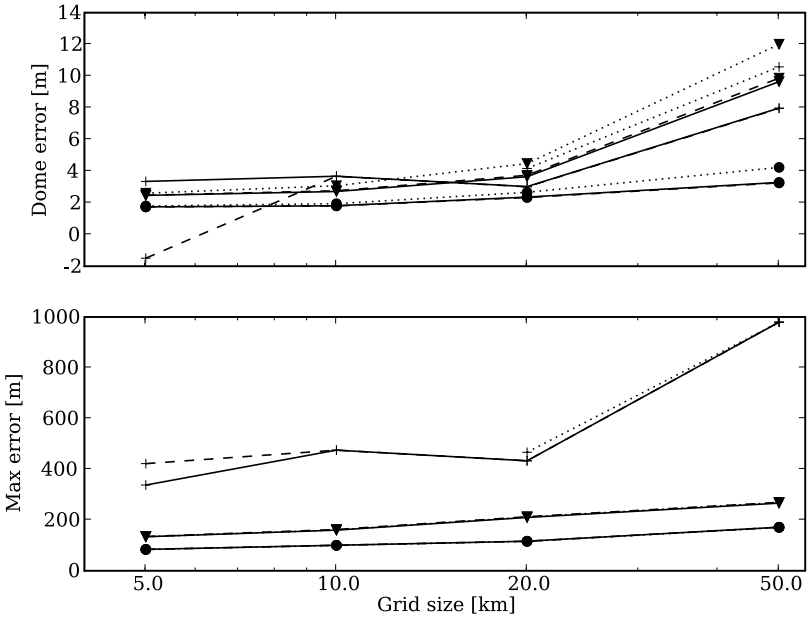

Figure 4. Overview of Glimmer verification runs. Tests B, C, and D are plotted with circles, inverted triangles, and crosses, respectively. Solid lines indicate the nonlinear solver, dashed lines indicate the linear solver, and dotted lines indicate the ADI solver. Thickness errors, at the center of the dome and the maximum error, are given for the final time step.

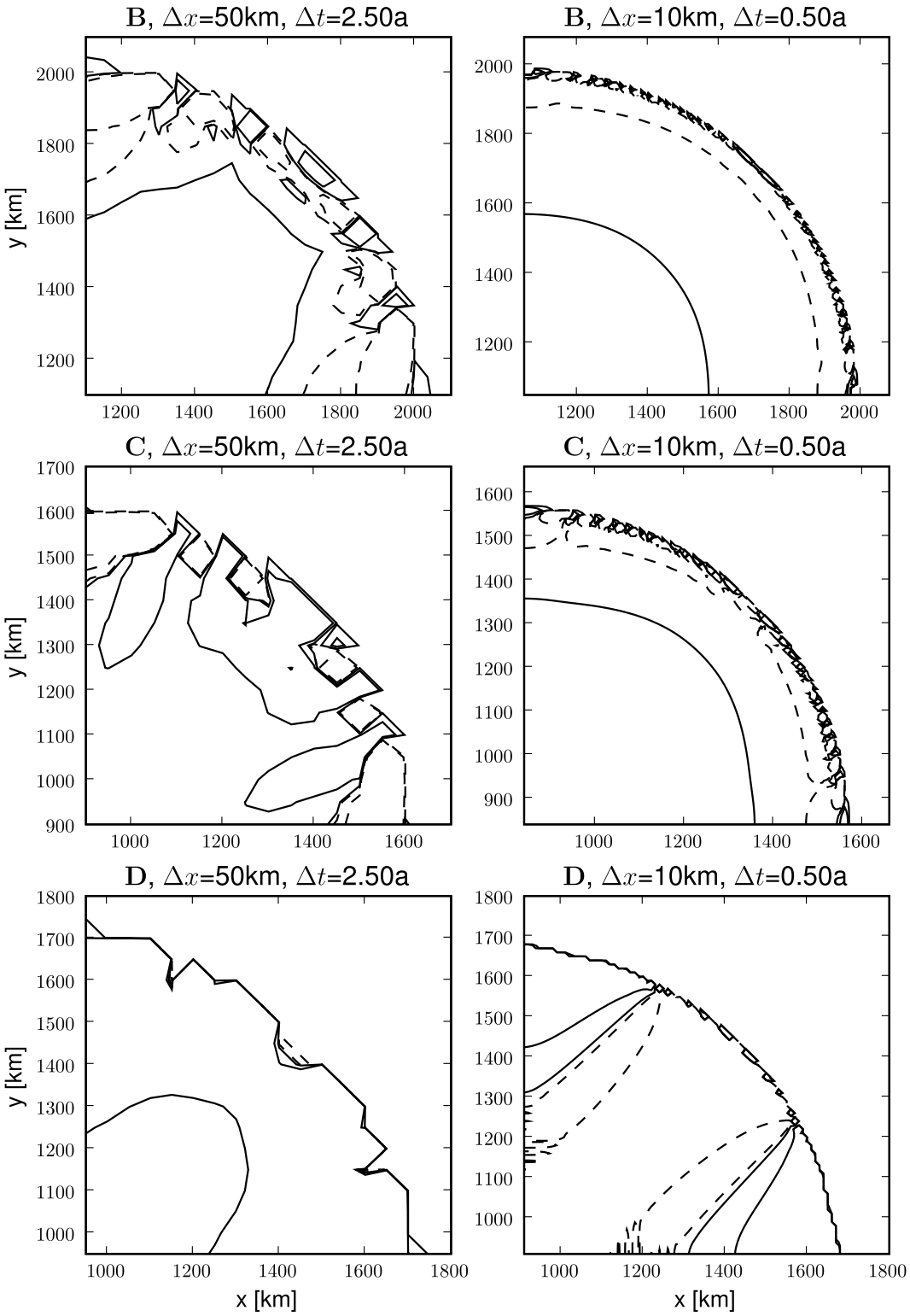

Figure 5. Snapshots at the final time step of the difference in ice height between the numerical solution using the linear solver and the exact solution. Contours are drawn at −10 m, −1 m, 1 m, and 10 m for the upper right quadrant of the domain. Positive values are solid, while negative values are dashed.

errors are concentrated at the margin, but that their influence reaches to the center of the ice sheet. In particular, Figure 6 shows that the sign of the largest spike in the error profile can vary between different runs, depending on the resolution. This supports the idea that the error is partly due to the shifting position of the margin as the resolution is changed.

[127] Second, the reduction of errors at higher resolution depends to some extent on choosing a sufficiently short time

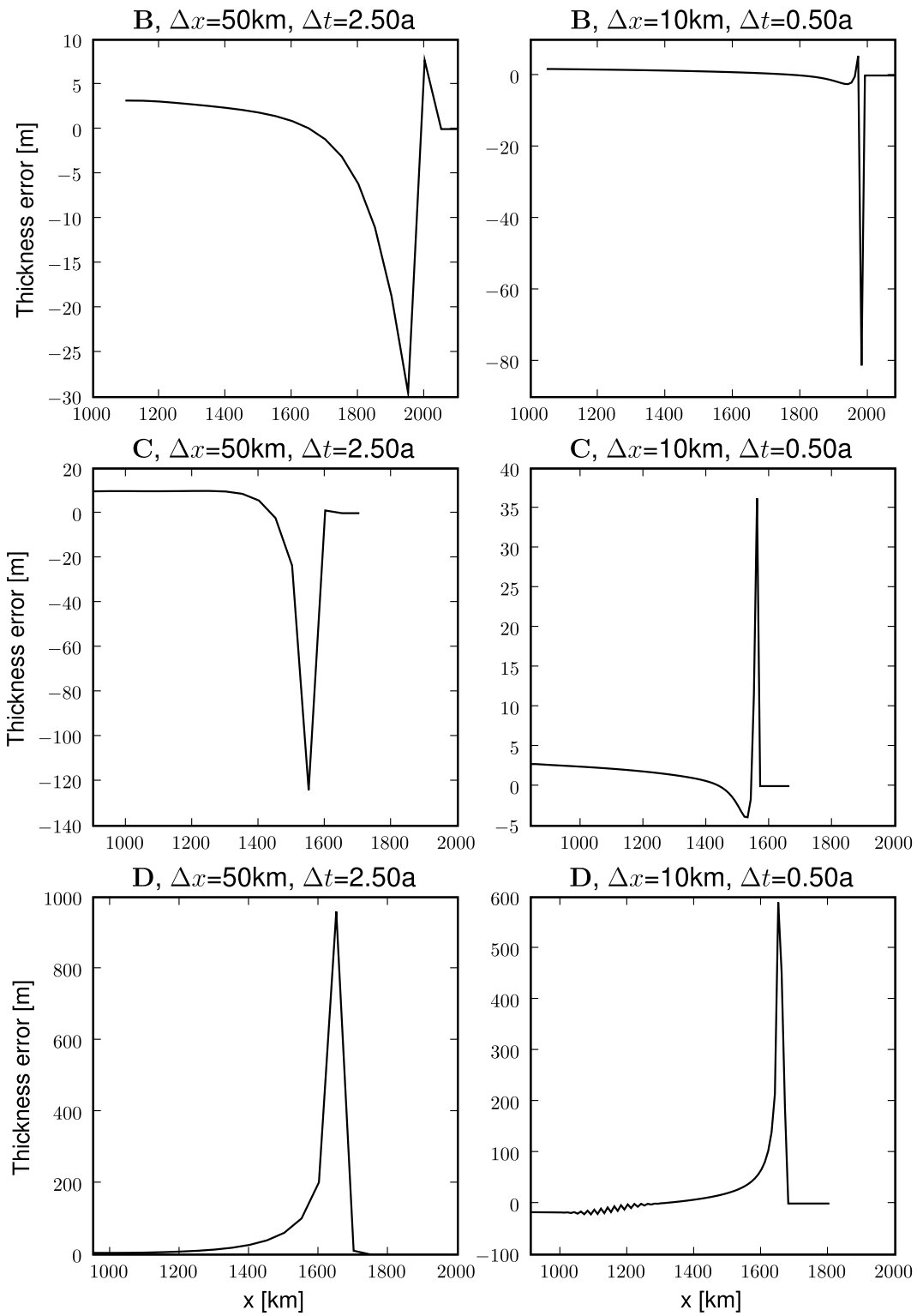

Figure 6. Snapshots at the final time step of the difference in ice height between the numerical solution using the linear solver and the exact solution. The thickness error along x through the center of the ice sheet is shown.

step. At higher resolutions, this may be difficult to do without making the model runs too time consuming to be practical; our own investigations indicate a dependence of the error on the time step size, especially when the linear semi-implicit scheme is used. The effect can be seen most clearly in Figure 4 in the results for test D with the linear solver. Both the dome error and the maximum error increase as the grid length is reduced from 10 km to 5 km; this is almost certainly due to the time step being too long.

[128] Despite these variations, the overall picture presented by the *Bueler et al.* [2005] tests is that the results from Glimmer converge toward the analytical solution. Together with the results from the EISMINT 1 and 2 intercomparisons, they constitute a robust verification of the Glimmer ice sheet model, and give us confidence that it can be used wherever the shallow ice approximation is valid.

8. Conclusions

[129] The Glimmer ice sheet model, presented in this paper, represents current best practice with regard to the simulation of large-scale ice sheet dynamics. The physics represented in the model, and the mathematical and numerical techniques used, are well established within the field; what distinguishes Glimmer from other models are the use of an open development paradigm, and the systematic verification of the model against recognized benchmarks. In addition, the novel structure of the model code gives Glimmer wide applicability within glaciology.

[130] We have shown in this paper that output from the core ice sheet model (GLIDE) compares well against the EISMINT benchmarks (levels one and two), and the exact isothermal solutions of *Bueler et al.* [2005]. These comparisons give Glimmer a level of verification and traceability which is lacking in many other models, and they significantly increase the confidence that can be placed in the output from the model.

[131] Further transparency is created by the free availability of the model source code, which may be compared against the description of the modeled physics and numerical methods used, given in this paper; during model development, this has allowed problems to be identified and fixed in a timely way. The community-based approach allows the most efficient communication of information to model users: with its international network of users and contributors, Glimmer is a true community model.

[132] In these respects, Glimmer is a step toward a more rigorous methodology for numerical modeling in the cryospheric sciences, as well as a useful model in its own right.

[133] **Acknowledgments.** This work was supported by the UK Natural Environment Research Council's (NERC) funding of the Centre for Polar Observation and Modelling and also as part of the GENIE project on NERC grant NER/T/S/2002/00221. Some of the work was also supported through an EU grant to Geoffrey Boulton at the University of Edinburgh. This grant and his collaboration in model development are gratefully acknowledged. M.H. would also like to acknowledge Sergei Zatsepin (University of Edinburgh). The authors would like to thank Felix Hebeler, Oliver Browne, Stewart Jameson, and other members of the Glimmer community for their assistance in the development of Glimmer, and the authors also thank the UK National eScience Centre for CVS hosting. Finally, we thank Jesse Johnson and Lev Tarasov for their detailed and helpful reviewer comments.

References

Abe-Ouchi, A., T. Segawa, and F. Saito (2007), Climatic Conditions for modelling the Northern Hemisphere ice sheets throughout the ice age cycle, *Clim. Past*, *3*, 423–438.

Alley, R. B., J. F. Bolzan, and I. M. Whillans (1982), Polar firn densification and grain growth, *Ann. Glaciol.*, *3*, 7–11.

Bar, M., and K. Fogel (2003), *Open Source Development With CVS*, Paraglyph, Scottsdale, Ariz.

Bauer, F. L. (1961), Algorithm 60: Romberg integration, *Commun. ACM*, *4*(6), 255.

Bueler, E., C. S. Lingle, J. A. Kallen-Brown, D. N. Covey, and L. N. Bowman (2005), Exact solutions and numerical verification for isothermal ice sheets, *J. Glaciol.*, *51*(173), 291–306.

Bueler, E., J. Brown, and C. Lingle (2007), Exact solutions to the thermomechanically coupled shallow-ice approximation: Effective tools for verification, *J. Glaciol.*, *53*(182), 499–516.

Calov, R., A. Ganopolski, M. Claussen, V. Petoukhov, and R. Greve (2005), Transient simulation of the last glacial inception. Part I: Glacial inception as a bifurcation in the climate system, *Clim. Dyn.*, *24*, 545–561.

Charbit, S., M. Kageyama, D. Roche, C. Ritz, and G. Ramstein (2005), Investigating the mechanisms leading to the deglaciation of past continental northern hemisphere ice sheets with the CLIMBER-GREMLINS coupled model, *Global Planet. Change*, *48*, 253–273.

Flowers, G. E., H. Björnsson, Á. Geirsdóttir, G. H. Miller, J. L. Black, and G. K. C. Clarke (2008), Holocene climate conditions and glacier variation in central Iceland from physical modelling and empirical evidence, *Quat. Sci. Rev.*, *27*, 797–813.

Glen, J. W. (1952), Experiments on the deformation of ice, *J. Glaciol.*, *2*, 111–114.

Greve, R. (1997), A continuum-mechanical formulation for shallow polythermal ice sheets, *Philos. Trans. Math. Phys. Eng. Sci.*, *355*, 921–974.

Hagdorn, M. K. M. (2008), *Simulation of the European Ice Sheets*, VDM Verlag Dr. Müller e.K., Saarbrücken, Germany.

Halfar, P. (1983), On the dynamics of the ice sheets 2, *J. Geophys. Res.*, *88*(C10), 6043–6051.

Hindmarsh, R. C. A. (1999), On the numerical computation of temperature in an ice sheet, *J. Glaciol.*, *45*(151), 568–574.

Hindmarsh, R. C. A., and K. Hutter (1988), Numerical fixed domain mapping solution of free-surface flows coupled with an evolving interior field, *Int. J. Numer. Anal. Methods Geomech.*, *12*, 437–459.

Hindmarsh, R. C. A., and E. Le Meur (2001), Dynamical processes involved in the retreat of marine ice sheets, *J. Glaciol.*, *47*(157), 271–282.

Hindmarsh, R. C. A., and A. J. Payne (1996), Time-step limits for stable solutions of the ice-sheet equation, *Ann. Glaciol.*, *23*, 74–85.

Holton, J. R. (1992), *An Introduction to Dynamic Meteorology*, *Int. Geophys. Ser.*, vol. 48, 3rd ed., Academic, New York.

Hutter, K. (1983), *Theoretical Glaciology: Mathematical Approaches to Geophysics*, D. Reidel, Dordrecht, Netherlands.

Huybrechts, P. (1986), A three-dimensional time-dependent numerical model for polar ice sheets: Some basic testing with a stable and efficient finite difference scheme, *Tech. Rep. 86-1*, Geogr. Inst. Vrije Univ. Brussel, Brussels, Belgium.

Huybrechts, P. (2002), Sea-level changes at the LGM from ice-dynamic reconstructions of the Greenland and Antarctic ice sheets during the glacial cycles, *Quat. Sci. Rev.*, *21*, 203–231.

Huybrechts, P., A. J. Payne, and EISMINT Intercomparison Group (1996), The EISMINT benchmarks for testing ice-sheet models, *Ann. Glaciol.*, *23*, 1–12.

Jenssen, D. (1977), A three-dimensional polar ice-sheet model, *J. Glaciol.*, *18*(80), 373–389.

Lambeck, K., and S. M. Nakiboglu (1980), Seamount loading and stress in the ocean lithosphere, *J. Geophys. Res.*, *85*(B11), 6403–6418.

Le Meur, E., and P. Huybrechts (1996), A comparison of different ways of dealing with isostasy: Examples from modelling the Antarctic ice sheet during the last glacial cycle, *Ann. Glaciol.*, *23*, 309–317.

Lenton, T. M., et al. (2007), Effects of atmospheric dynamics and ocean resolution on bi-stability of the thermohaline circulation examined using the grid enabled integrated earth system modelling (GENIE) framework, *Clim. Dyn.*, *29*(6), 591–613, doi:10.1007/s00382-007-0254-9.

Leysinger Vieli, G. J.-M. C., and G. H. Gudmundsson (2004), On estimating length fluctuations of glaciers caused by changes in climatic forcing, *J. Geophys. Res.*, *109*, F01007, doi:10.1029/2003JF000027.

Mahaffy, M. W. (1976), A three-dimensional numerical model of ice sheets: Tests on the Barnes Ice Cap, Northwest Territories, *J. Geophys. Res.*, *81*(6), 1059–1066.

Metcalf, M., and J. Reid (1999), *FORTRAN 90/95 Explained*, 2nd ed., Oxford Univ. Press, Oxford, U. K.

Milne, G. A., J. L. Davis, J. X. Mitrovica, H.-G. Scherneck, J. M. Johansson, M. Vermeer, and H. Koivula (2001), Space-geodetic constraints on glacial isostatic adjustment in Fennoscandia, *Science*, *291*, 2381–2385.

Nye, J. F. (1953), The flow law of ice from measurements in glacier tunnels, laboratory experiments and the Jungfraufirn borehole experiments, *Proc. R. Soc. London, Ser. A*, *219*, 477–489.

Paterson, W. S. B. (1994), *The Physics of Glaciers*, 3rd ed., Butterworth-Heinemann, Oxford, U. K.

Pattyn, F. (2003), A new three-dimensional higher-order thermomechanical ice sheet model: Basic sensitivity, ice stream development, and ice flow across subglacial lakes, *J. Geophys. Res.*, *108*(B8), 2382, doi:10.1029/2002JB002329.

Payne, A. J. (1995), Limit cycles in the basal thermal regime of ice sheets, *J. Geophys. Res.*, *100*(B3), 4249–4263.
Payne, A. J. (1999), A thermomechanical model of ice flow in West Antarctica, *Clim. Dyn.*, *15*, 115–125.
Payne, A. J., and P. W. Dongelmans (1997), Self-organisation in the thermomechanical flow of ice sheets, *J. Geophys. Res.*, *102*(B6), 12,219–12,233.
Payne, A. J., et al. (2000), Results from the EISMINT model intercomparison: The effects of thermomechanical coupling, *J. Glaciol.*, *46*(153), 227–238.
Peltier, W. R., D. L. Goldsby, D. L. Kohlstedt, and L. Tarasov (2000), Ice-age ice-sheet rheology: Constraints from the Last Glacial Maximum form of the Laurentide ice sheet, *Ann. Glaciol.*, *30*, 163–176.
Pollard, D., and S. L. Thompson (1997), Driving a high-resolution dynamic ice-sheet model with GCM climate: Ice-sheet initiation at 116,000 BP, *Ann. Glaciol.*, *25*, 296–304.
Press, W., S. Teukolsky, W. Vetterling, and B. Flannery (1992), *Numerical Recipes in FORTRAN*, 2nd ed., Cambridge Univ. Press, Cambridge, U. K.
Reeh, N. (1991), Parameterization of melt rate and surface temperature on the Greenland Ice Sheet, *Polarforschung*, *59*(3), 113–128.
Rew, R., and G. Davis (1990), NetCDF: An interface for scientific data access, *IEEE Trans. Comput. Graphics Appl.*, *10*(4), 76–82.
Ritz, C. (1987), Time dependent boundary conditions for calculation of temperature fields in ice sheets, in *The Physical Basis of Ice Sheet Modelling*, *IAHS Publ.*, *170*, 207–216.
Saito, F., and A. Abe-Ouchi (2005), Sensitivity of Greenland ice sheet simulation to the numerical procedure employed for ice dynamics, *Ann. Glaciol.*, *42*, 331–336.
Seager, M. (1988), A SLAP for the masses, *Tech. Rep. UCRL-100267*, Lawrence Livermore Nat. Lab., Livermore, Calif.
Tarasov, L., and W. R. Peltier (1999), Impact of thermomechanical ice sheet coupling on a model of the 100kyr ice age cycle, *J. Geophys. Res.*, *104*(D8), 9517–9545.
Tarasov, L., and W. R. Peltier (2000), Laurentide ice sheet aspect ratio in models based on Glen's flow law, *Ann. Glaciol.*, *30*, 177–186.
Van den Berg, J., R. S. W. Van de Wal, and J. Oerlemans (2006), Effects of spatial discretization in ice-sheet modelling using the shallow-ice approximation, *J. Glaciol.*, *52*(176), 89–98.
Vettoretti, G., and W. R. Peltier (2004), Sensitivity of glacial inception to orbital and greenhouse gas climate forcing, *Quat. Sci. Rev.*, *23*, 499–519.
Vieli, A., and A. J. Payne (2005), Assessing the ability of numerical ice sheet models to simulate grounding line migration, *J. Geophys. Res.*, *110*, F01003, doi:10.1029/2004JF000202.

M. Hagdorn and N. R. J. Hulton, School of GeoSciences, University of Edinburgh, Grant Institute, The King's Buildings, West Mains Road, Edinburgh EH9 3JW, UK.

A. J. Payne, Centre for Polar Observation and Modelling, School of Geographical Sciences, University of Bristol, University Road, Bristol BS8 1SS, UK.

I. C. Rutt, School of the Environment and Society, Swansea University, Singleton Park, Swansea SA2 8PP, UK. (i.c.rutt@swansea.ac.uk)